Peatlands and their carbon dynamics in northern high latitudes from 1990 to 2300: A process-based biogeochemistry model analysis

Bailu Zhao[1], Qianlai Zhuang[1,2]

[1] Department of Earth, Atmospheric, and Planetary Sciences, Purdue University, West Lafayette, IN 47907, USA

[2] Department of Agronomy, Purdue University, West Lafayette, IN 47907, USA

Correspondence to: Qianlai Zhuang (qzhuang@purdue.edu)

Abstract. Northern peatlands have been a large C sink during the Holocene, but whether they will keep being a C sink under future climate change is uncertain. This study simulates the responses of northern peatlands to future climate until 2300 with a Peatland version Terrestrial Ecosystem Model (PTEM). The simulations are driven with two sets of CMIP5 climate data (IPSL-CM5A-LR and bcc-csm1-1) under three warming scenarios (RCP2.6, 4.5 and 8.5). Peatland area expansion, shrinkage and C accumulation and decomposition are modelled. In the 21st century, northern peatlands are projected to be a C source of 1.2-13.3 Pg C under all climate scenarios except for RCP 2.6 of bcc-csm1-1 (a sink of 0.8 Pg C). During 2100-2300, northern peatlands under all scenarios are a C source under IPSL-CM5A-LR scenarios, being larger sources than bcc-csm1-1 scenarios (5.9-118.3 vs. 0.7-87.6 Pg C). C sources are attributed to: 1) peatland water table depth (WTD) becomes deeper and permafrost thaw increases decomposition rate; 2) net primary production (NPP) does not increase much as climate warms because peat drying suppresses net N mineralization; and 3) as WTD deepens, peatlands switches from moss-herbaceous dominated to moss-woody dominated, while woody plants require more N for productivity. Under IPSL-CM5A-LR scenarios, northern peatlands remain as a C sink until pan-Arctic annual temperature reaches -2.6 - -2.89°C, while this threshold is -2.09 - -2.35°C under bcc-csm1-1 scenarios. This study predicts an northern peatland sink to source shift in around 2050, earlier than previous estimates of after 2100 and emphasizes the vulnerability of northern peatlands to climate change.

1 Introduction

Peatlands are an ecosystem type that characteristically has more than 30cm peat thickness comprised of more than 30% organic materials within the peat layer (Finlayson and Milton, 2018). The formation of this thick organic soil layer requires wet and low oxygen conditions that prevent dead plant litter from being fully decomposed (Finlayson and Milton, 2018). Around 85% of global peatlands C storage is in northern high latitude regions (415±150 Pg C) (Nichols and Peteet, 2019; Turunen et al., 2002) where low temperature and relatively high precipitation create favorable conditions for peat accumulation (Xu et al., 2018; Hugelius et al., 2020).

Peatlands are vulnerable to disturbances induced by climate warming (Loisel et al., 2021), especially when the warming in the Arctic region is almost three times as much as the global average (GISTEMP-Team., 2021). First, warming

influences northern terrestrial ecosystem vegetation productivity by increasing spring photosynthesis, triggering spring onset earlier and delaying autumn green-down (Piao et al., 2008; Helbig et al., 2017, Richardson et al., 2018). Second, warming could induce drier Arctic conditions with 21% of lake count and 2% of lake area decrease found from the 1960s to present (Finger Higgens et al., 2019), and peatlands water table drawdown would result in net increase of greenhouse gas emissions of 0.86 Gt CO_2-eq $\cdot$yr^{-1} by 2100 (Huang et al., 2021). Third, decomposition rate increases under higher temperature and previous studies found positive linear correlations between warming and net C loss rate of 31.3 gC$\cdot$m$^{-2}\cdot$year$^{-1}\cdot$°C^{-1} (Hanson et al., 2020). Fourth, permafrost thaw under warming conditions will expose previously-frozen C for dissolving and decomposition (Gandois et al., 2019). To date, multiple modelling studies have explored northern peatland responses to future climate changes (Loisel et al., 2021; Qiu et al., 2020; Chaudhary et al., 2020; Müller and Joos, 2021). However, the projection of northern peatland C sink capacity during the 21st century is highly diverse including sink-to-source switch (Chaudhary et al., 2017; Müller and Joos, 2021), higher sink capacity under mild climate changes (Qiu et al., 2020), and the reduced C sink capacity (Chaudhary et al., 2020).

Given the uncertainties of northern peatlands response to future climate changes, modelling peatland C dynamics including peatland extent changes could improve the accuracy of future projection. In this study, a process-base model, the Peatland Terrestrial Ecosystem Model (PTEM 2.2), is used to address this issue. PTEM 2.0 has been modified in terms of plant functional type (PFT), peat accumulation and decomposition, fen-bog transition and soil thermal module to better represent peatland ecosystem processes (Zhao et al., 2022b). The revised PTEM 2.0 is able to capture peat core age-depth profile at site level (Zhao et al., 2022b) and has been further modified and applied to simulate Holocene (PTEM 2.1, 15ka BP - 1990) pan-Arctic peatland accumulation and expansion at 0.5° resolution (Zhao et al., 2022a). The estimated pan-Arctic peatland C stock is 396-421 Pg C and Holocene average C accumulation rate (CAR) is 22.9 g C$\cdot$m^{-2} yr^{-1} (Zhao et al., 2022a). The values and spatial pattern of soil C stock are in a close agreement with Qiu et al. (2019), Hugelius et al. (2020), Spahni et al. (2013) and Hugelius et al. (2013), and the values and temporal pattern of CAR are consistent with Loisel et al. (2014), Chaudhary et al. (2020) and Nichols and Peteet (2019). In this study, the results of the Holocene simulation are used as the initial condition for the future simulation.

The methods used in Holocene simulation can not be applied directly to future simulation due to two issues. First, previous studies on future peatland C dynamics are mostly based on fixed peatland extent (Loisel et al., 2021; Chaudhary et al., 2020), but future peatland extent is likely to vary under climate change. To address this issue, we enhance PTEM 2.2 to simulate wetland dynamic extent during 1990-2300 at sub-grid cell scales. Notably, although the spatially explicit peat expansion process was considered in the Holocene simulation, the sub-grid cell expansion trend was simply derived from the fitted curve of existing pan-Arctic peat basal dates (Zhao et al., 2022a). It is problematic to apply this fitted trend to future simulation since severe climate changes may interrupt the Holocene peat expansion pattern. Therefore, a different approach of estimating peatland extent needs to be developed for future simulation.

Second, in PTEM 2.2, peatland water table depth (WTD) and nutrient availability is influenced by run-on, which is the water input from ground water or adjacent water bodies into the peatlands. Previous PTEM 2.1 assumes run-on is a

function of peat thickness, and the theoretically maximum run-on corresponding with 0cm peat thickness. Under relatively stable climate conditions during the Holocene after peat initiation, the theoretically maximum run-on is assumed to be a constant (i.e., parameter) and thereby run-on solely depends on peat thickness (Zhao et al., 2022a). However, when climate becomes wetter or drier in the future, the theoretically maximum run-on could vary significantly and the original PTEM 2.1 assumption becomes problematic. Therefore, it is necessary to revise the hydrology module of PTEM 2.2 such that run-on could respond to climate change.

To address these two issues, a TOPMODEL approach is used (Lu and Zhuang (2012). The TOPMODEL approach downscales coarse grid cell WTD into finer resolutions given the sub-grid-cell topographic wetness index (TWI) and decay parameter (*f*) (Beven and Kirkby, 1979). Previous studies have combined TEM, TOPMODEL and variable infiltration capacity (VIC) model to estimate Alaska Yukon river basin methane emissions using 1km resolution WTD interpolated from 30km resolution (e.g., Lu and Zhuang (2012)). By applying TOPMODEL, we are able to estimate the dynamics of a) sub-grid-cell WTD; b) the spatially explicit wetland fraction defined by annual WTD threshold (25cm, Fan et al. (2013)); c) sub grid-cell peat accumulation and decomposition given interpolated WTD; and d) the spatially explicit peatland fraction defined by peat thickness threshold (30cm, Finlayson and Milton (2018)). Furthermore, soil moisture can be estimated from WTD, with which we can estimate run-on from the difference between interpolated WTD and simulated WTD without run-on.

With peatland dynamics being simulated both horizontally (i.e., peatlands expansion and shrink) and vertically (i.e., peat accumulation and decomposition), this study aims to answer the following questions: a) how will the C sink of pan-Arctic peatlands change during 1990-2300? b) What are the major drivers for these changes? c) How does the pan-Arctic peatlands C sink respond to unit temperature and precipitation increase? and d) What is the threshold temperature and precipitation for pan-Arctic peatland C sink and source shift?

2 Methods

In this study, two CMIP5 climate model products (IPSL-CM5A-LR and bcc-csm1-1) are selected as climate inputs, with three warming scenarios considered (RCP 2.6, RCP 4.5 and RCP 8.5). The simulation is divided into two parts: 1) simulating grid cell average WTD with PTEM 2.2 and interpolating grid cell WTD into sub-grid cell scale with the TOPMODEL approach; and 2) simulating sub-grid cell scale peat accumulation and decomposition in current and potential peatland regions (Figure 1). Although this study aims at the peatland C expansion, shrinkage, accumulation and decomposition after 1990, the simulations start in 1940. The simulation during 1940-1990 works as spin up process and is also used for calibration against historical data.

2.1 Selection of climate input data

In the previous PTEM 2.0 site-level simulation, among many CMIP5 data products, IPSL-CM5A-LR product was selected as climate input because it provides long temporal coverage (1850-2300) for RCP 2.6, RCP 4.5 and RCP 8.5

scenarios (Zhao et al., 2022b). In addition, it shows a good agreement with Climatic Research Unit (CRU) temperature in Eurasia and low biases in historical temperature and precipitation in North America (Miao et al., 2014; Sheffield et al., 2013). However, IPSL-CM5A-LR product also shows more extreme warming than the other CMIP5 products, especially under RCP 8.5 (Palmer et al., 2018). To address the uncertainty caused by climate inputs, another CMIP5 product, bcc-csm1-1, covering 1850-2300, three RCP scenarios, projecting milder future climate warming, is selected. The comparison of two forcing datasets is provided in SI Table1. In order to run PTEM 2.2, temperature, precipitation, cloudiness and vapor pressure are required. Neither of IPSL-CM5A-LR and bcc-csm1-1 model provides vapor pressure data, which are thus calculated with temperature and relative humidity (Zhao et al., 2022b). Both climate products are bias-corrected to Climatic Research Unit data (v4.03, Harris et al. (2014)) during 1940-1990 as described in Zhao et al. (2022b). The bias correction makes sure that the difference in future simulations under two climate inputs are mostly introduced by the different level of post-1990 warming, rather than the difference in their historical records before 1990.

Table 1. List of abbreviations

Abbreviation	Full name
PTEM	Peatland terrestrial ecosystem model
CMIP5	Coupled Model Intercomparison Project Phase 5
RCP	Representative Concentration Pathway
WTD	Water table depth
CAR	C accumulation rate
VIC	Variable Infiltration Capacity model
TWI	Topographic wetness index
PFT	Plant functional type
EET	Evapotranspiration
PET	Potential evapotranspiration
PEST	Model-Independent Parameter Estimation and Uncertainty Analysis
NPP	Net primary productivity
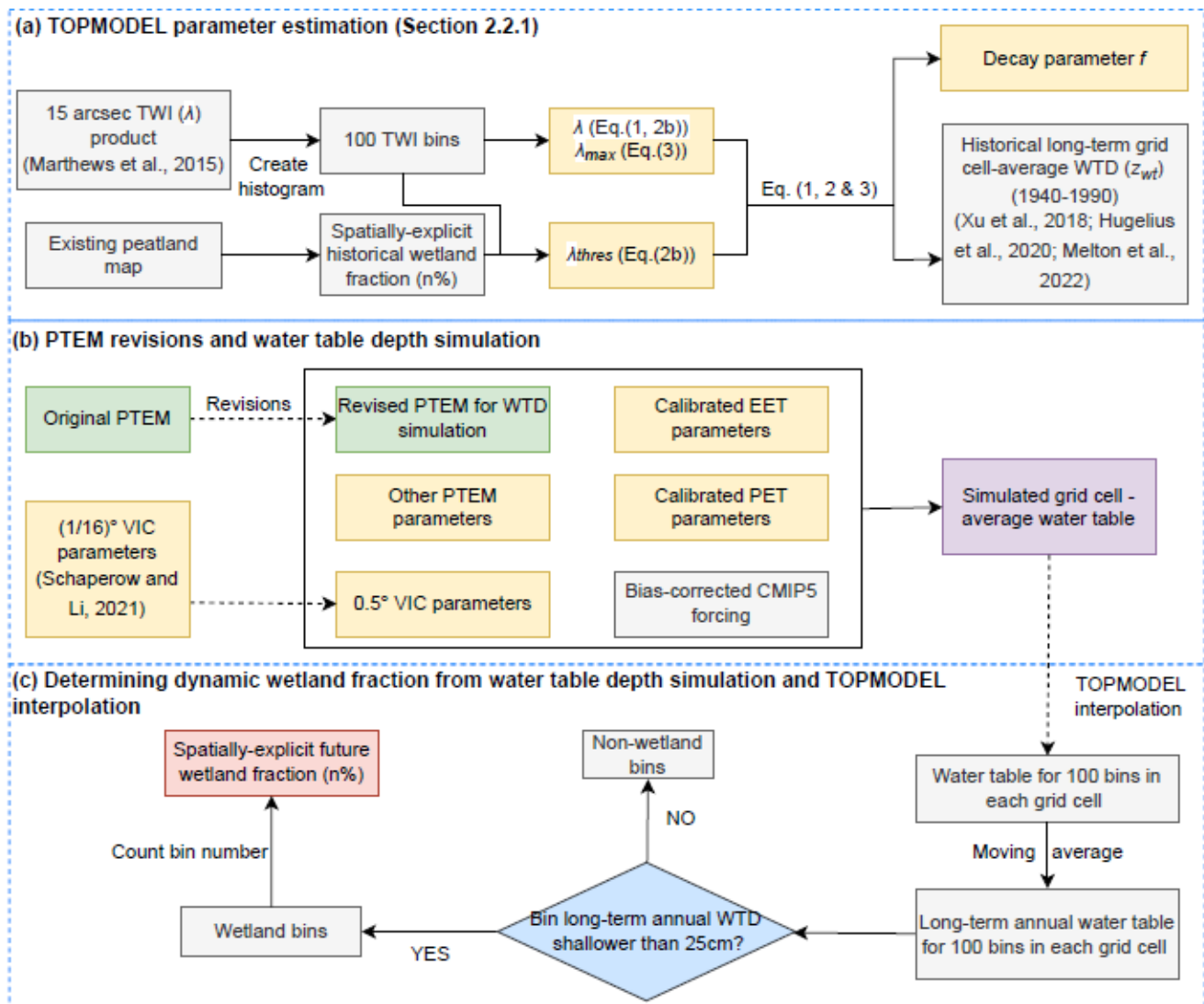
Figure 1. Flow chart of Method Section 2.2.

2.2 Future grid cell average WTD simulation

2.2.1 TOPMODEL parameter estimation

In this study, the peatland condition in 1940 derived from previous Holocene simulation is used as the initial condition for future peatland simulations (1940-2300) (Zhao et al., 2022a). In order to be consistent with the Holocene simulation, before running future WTD simulation, it is necessary to make sure that interpolating the PTEM-simulated recent WTD by TOPMODEL could derive the wetland extent as shown in the end of the Holocene simulation. In particular, 'recent' in this study refers to 1940-1990, and wetlands are defined as the region with long-term annual WTD shallower than

121 25cm (Fan et al., 2013). To satisfy this requirement, the TOPMODEL parameters need to be estimated before WTD

122 simulation (Figure 1(a)). TOPMODEL describes sub-grid cell WTD variation with topography. The topography effects on

123 the local WTD are estimated with topographic wetness index (TWI) values, the larger TWI values indicate the shallower

124 WTD and higher flooding probability (Stocker et al., 2014). In order to estimate sub-grid cell wetland and peatland

125 conditions at 1% accuracy, each $0.5°\times0.5°$ grid cell is divided into 100 bins by the TWI histogram (Figure 1 (a), SI Figure1).

126 With global terrestrial TWI values available at 15 arcsec resolution (Marthews et al., 2015), each bin is composed of 36 TWI

127 values where water bodies have null values (SI Figure1). For bin i within a given grid cell:

$$z_{wti} = z_{wt} - \frac{1}{f} \times (k_i - \lambda) \tag{1}$$

129 Where z_{wti} is the WTD of bin i, k_i is the average TWI of bin i, λ is the grid cell average TWI, z_{wt} is the grid cell

130 average WTD and f is the decay parameter. In Eq. (1), the parameters need to be estimated are z_{wt} and f. In particular, the

131 z_{wt} here refers to the 50-year average WTD during 1940-1990. z_{wt} and f values are calculated as:

$$\begin{cases} f = 2.6 & \text{(2a)} \\ z_{wt-thres} = z_{wt} + \frac{1}{f}(\lambda_{thres} - \lambda) & \text{(2b)} \end{cases}$$

133

134 Where f value is from Kleinen et al. (2020). $z_{wt-thres}$ is the threshold WTD of wetlands (i.e., -0.25m) and λ_{thres} is

135 the TWI value corresponding to $z_{wt-thres}$. For a given grid cell where wetland abundance is n% (n is an integer), λ_{thres} is

136 the TWI value of the n-th largest TWI values among 100 bins. The spatially explicit wetland fraction (n%) during 1940-1990

137 is consistent with the wetland fraction in 1990 in the Holocene simulation, which is the average value of three peatland maps

138 covering the pan-Arctic region (Xu et al., 2018; Hugelius et al., 2020; Melton et al., 2022). The shallowest WTD in each grid

139 cell is:

$$z_{wt-max} = z_{wt} + \frac{1}{f}(\lambda_{max} - \lambda) \tag{3}$$

141 Where λ_{max} is the maximum TWI value in 100 bins. If z_{wt-max} is greater than zero (i.e., above surface), z_{wt-max}

142 is assumed to be -0.01m, and z_{wt} and f values are calculated by Eq. (2b) and Eq. (3). Otherwise, z_{wt} and f values are

143 calculated by Eq. (2a) and Eq. (2b).

144 **2.2.2 PTEM revisions**

145 The PTEM 2.1 used in pan-Arctic Holocene simulations is able to estimate the wetland WTD in a given grid cell,

146 while not the grid-cell average WTD composed of both wetland and non-wetland land covers (Zhao et al., 2022a). In order

147 to simulate the grid-cell average WTD, PTEM 2.1 is revised by applying some of the algorithms from VIC model (Figure

148 1(b)). VIC model was developed by Liang et al. (1994) and has been updated to version 5 (VIC-5, Hamman et al. (2018)).

149 Compared with the hydrology module of PTEM 2.1, VIC has the same soil vertical structure of three layers. The major

150 hydrological processes including canopy interception of precipitation, infiltration, gravity-driven vertical flow,

151 evapotranspiration, upper soil layer evaporation, effect of frozen-thaw on soil moisture are considered in both models (Liang

152 et al., 1994; Zhuang et al., 2002). With similar structure, processes and variables, it is possible to apply some of VIC

153   algorithms to PTEM 2.1. In particular, the algorithms of surface runoff, vertical flow from upper to lower layers, the

154   computation of base flow and the estimation of WTD from given soil moisture are added to PTEM 2.1. The computation of

155   surface runoff in VIC is based on the Xinanjiang model that assumes runoff is the amount of precipitation that falls on the

156   saturated fraction of a grid cell (Zhao et al., 1980). The relationship between soil water storage and saturated fraction is

157   given by:

158    $i = i_m[1 - (1 - A)^{1/B}]$ (4)

159   Where A is the fraction of the grid cell that the infiltration capacity (i.e., the possible maximum depth of water

160   stored in soil column given area fraction) is less than i, i_m is the maximum infiltration capacity within the given grid cell,

161   and B is a shape parameter (Wood et al., 1992). The calculation of the uppermost layer runoff given precipitation and the

162   initial soil moisture is well documented in Wood et al. (1992) (Eq. (1-3)) and Liang et al. (1994) (Eq. (13), Eq. (17-18)). In

163   addition, gravity-driven water flow from upper to lower layers is given by Liang et al. (1994) (Eq. (18-20)) based on upper

164   layer soil moisture, residual moisture content, pore size distribution index and the hydraulic conductivity estimated from

165   Brooks (1965). Following VIC, PTEM 2.2 also assumes base flow only happens in the bottom soil layer. The computation of

166   base flow in VIC is derived from the model in Franchini and Pacciani (1991) and the equations are listed in Liang et al.

167   (1994) (Eq. (21)). Computing WTD given soil moisture was first used in VIC 4.1.2 (Bohn et al., 2013). Edited from VIC-5,

168   the WTD-soil moisture relationship in PTEM 2.2 is given by:

169    $W_{tot} = W_{avg} \times (SM_{max} - SM_{res}) + SM_{res}$ (5)

170   Where W_{tot} is the total soil moisture of three layers (mm), W_{avg} is the average relative soil moisture, SM_{max} is the

171   maximum soil moisture (mm) and SM_{res} is the residual soil moisture (mm). With SM_{max} and SM_{res} being spatially explicit

172   parameters, W_{avg} is:

173    $W_{avg} = (D_{tot} - z_{wt} - \frac{b}{b-1} \times bubble \times (1 - \left(\frac{z_{wt}+bubble}{bubble}\right)^{\frac{b-1}{b}}))/D_{tot}$ (6)

174   Where D_{tot} is the total depth of soil layer (cm), z_{wt} is given WTD (cm below surface), $bubble$ is the bubbling

175   pressure (cm), b is the parameter:

176    $b = 0.5 \times (expt - 3)$ (7)

177   Where $expt$ is the exponent parameter from Brooks-Corey relationship, and is always greater than 3 (Rawls et al.,

178   1992). In PTEM 2.2, the spatially explicit relationship between WTD and total soil moisture is given by Eq. (5-7) at 5cm

179   WTD interval. During simulation, PTEM 2.2 calculates the total soil moisture and finds the corresponding WTD. In case of

180   soil moisture does not correspond with any 5-cm interval WTD, PTEM 2.2 will find the closest upper and lower soil

181   moisture values in the soil moisture-WTD profile and interpolate from the upper and lower WTD values.

182   In site-level and Holocene simulations, there are three PFTs in PTEM 2.0 and 2.1: moss, herbaceous plant and

183   shrub (Zhao et al., 2022b). However, trees are also an important PFT in northern peatlands (Hanson et al., 2020). Therefore,

184   in both grid-cell average WTD and sub-grid cell peatland simulations, it is necessary to include trees as a PFT. In particular,

185   the vegetation C and N pool in PTEM 2.2 are now divided into four sub-pools: moss, herbaceous plant, shrub and tree. The

186 dominance of these four PFTs are determined by WTD and their maximum possible productivity. The litter fall from four
187 PFTs becomes the input of soil C and N, and the decomposition ability of litter is influenced by the fraction of litter origin
188 from each PFT. The calculations of C and N cycles of trees are the same as the other three PFTs, although controlled by
189 different PFT-specific parameters. The detailed description and equations are documented in Zhao et al. (2022b).

190 The calculation of evapotranspiration (EET) of vascular plants in PTEM 2.2 is derived from Food and Agriculture
191 Organization (FAO) algorithm for calculating crop EET (Allen et al., 1998):

192 $$EET = PET \times k_c \times foliage + E_{soil} \times (1 - foliage) \qquad (8)$$

193 Where PET is the potential evapotranspiration given by Penman-Monteith model in PTEM 2.2, k_c is a coefficient,
194 E_{soil} is the evaporation from the top soil layer and $foliage$ is a PTEM 2.2 variable describing the relative abundance of leaf
195 biomass (0-1). The $E_{soil} \times (1 - foliage)$ is used to represent the evapotranspiration from the top hydrology layer, which is
196 assumed to be a moss layer in PTEM. Although the Food and Agriculture Organization algorithm is widely applied in
197 estimating crop EET, it is also proved applicable to shrubland, grassland and forest (Liu et al., 2017). In PTEM 2.2, k_c is
198 calculated as:

199 $$k_c = \sum_{i=1}^{3} k_{c-pft} \times w_{pft} \qquad (9)$$

200 Where three vascular PFTs are considered influential to EET (i.e., herbaceous plant, shrub and tree), k_{c-pft} is the
201 spatially explicit coefficient for given PFT, and w_{pft} is the weight of given PFT estimated from its dominance:

202 $$w_{pft} = \frac{VEGC_{pft}}{\sum_{i=1}^{3} VEGC_{pft}} \qquad (10)$$

203 Where $VEGC_{pft}$ is the vegetation C of given PFT, and only three vascular PFTs are used for weight calculation. In
204 WTD simulation, we assume no run-on from adjacent grid cells, thereby the grid cell water balance is:

205 $$\Delta SM = P - R_{off} - B - EET \qquad (11)$$

206 Where ΔSM is the change of soil moisture, P is precipitation, R_{off} is surface run-off and B is the bottom layer base
207 flow.

2.2.3 Grid cell average WTD simulation and post-processing

209 Adding VIC algorithms to PTEM 2.2 requires VIC parameters at 0.5° resolution. These parameters include variable
210 infiltration curve parameter (binfilt), maximum velocity of base flow (Dsmax), fraction of Dsmax where non-linear base
211 flow begins (Ds), fraction of maximum soil moisture where non-linear base flow occurs (Ws), exponent used in base flow
212 curve (c), expt in Eq. (7), saturated hydrologic conductivity (Ksat), depth of three soil layers (depth), bubbling pressure of
213 soil layers (bubble), bulk density of soil layers (bulk_density) and soil particle density (soil_density). These parameter values
214 are available globally at (1/16)° resolution (Schaperow and Li, 2021) and are aggregated into 0.5° resolution in this study. To
215 run PTEM 2.2, in addition to the climate inputs, the historical (1940-1990) CO_2 concentration (ppm) is derived from TraCE
216 21ka dataset (He, 2011). The CO_2 concentration for three RCP scenarios (1991-2300) is provided by Meinshausen et al.
217 (2011). Spatially explicit soil texture (FAO/UNESCO, 1974) and elevation (Zhuang et al., 2002) were also required (Figure
218 1(b)).

219   Before conducting WTD simulation, spatially explicit calibration for annual PET and k_{c-pft} are conducted.
220 Spatially explicit calibration for annual PET is conducted because the original PTEM 2.1 parameters estimate unreasonably
221 large PET. Therefore, the global aridity index and potential evapo-transpiration (ET0) database v3 (Zomer and Trabucco,
222 2022) is selected as a reference. The dataset is selected because its annual PET is the long-term value of 1970-2000, which
223 can be the approximate reference to the PET during 1940-1990 in this study. In addition, the reference dataset is also based
224 on Penman-Monteith model but with more detailed estimation on the parameters than PTEM (Zomer and Trabucco, 2022).
225 The 30 arcsec resolution reference PET is aggregated into 0.5° resolution for calibration. The spatially explicit Penman-
226 Monteith parameters in PTEM 2.2 are calibrated with PEST (v17.2 for Linux). Since both reference dataset and PTEM 2.2
227 estimate PET with the same model, the calibration result is close to the reference for both IPSL-CM5A-LR and bcc-csm1-1
228 climate inputs (SI Figure 2).

229   After PET calibration, the spatially explicit calibration for k_{c-pft} is conducted such that the 50-year WTD is
230 consistent with the z_{wt} calculated by Eq. (2-3). Same as PET calibration, spatially explicit k_{c-pft} values are also calibrated
231 by PEST (v17.2 for Linux). The wetland abundance in the end of the Holocene simulation (i.e., reference dataset) (Xu et al.,
232 2018; Hugelius et al., 2020; Melton et al., 2022) and the wetland abundance interpolated by TOPMODEL from calibrated
233 WTD (average of 1940-1990) is shown in Figure 2. Notably, the extent of pan-Arctic peatlands is used as an approximation
234 of pan-Arctic wetlands because the northern peatland extent is estimated to be 2.9-3.3 Mkm², with an average of 3.05 Mkm²
235 (Xu et al., 2018; Hugelius et al., 2020; Melton et al., 2022); while the northern wetland extent is estimated to be 3.2 Mkm²
236 (Olefeldt et al. 2021), indicating northern wetlands are dominated by northern peatlands. In addition, the peatland coverage
237 from Xu et al. (2018) and Hugelius et al.(2020) both include the shallow peats (<30cm), which is classified as wetlands
238 rather than peatlands in this study. Since each grid cell is divided into 100 bins by TWI values, the minimum wetland
239 abundance is 1%. In this study, the grid cells with less than 1% wetland are not used for peat simulation. Leaving out the grid
240 cells with less than 1% wetlands, the pan-Arctic wetlands area for the reference dataset is 2.93 Mkm², the calibrated
241 wetlands area with IPSL-CM5A-LR forcing input is 2.81 million km², and with bcc-csm1-1 forcing input is 2.86 million km²
242 (Figure 2).

243   After calibration, the WTD simulation is conducted for 1940-2300 at 0.5° resolution (Figure 1 (b)). Notably, WTD
244 simulation only aims at estimating grid cell average WTD and the peat accumulation and decomposition processes are not
245 simulated. The grid cell average WTD during 1940-2300 is interpolated by TOPMODEL using the parameters calculated in
246 Section 2.2.1 (Figure 1(c)). The changes of wetlands extent during 1990-2300 under IPSL-CM5A-LR and bcc-csm1-1
247 forcing inputs are presented in SI Figure 3 and 4.

248
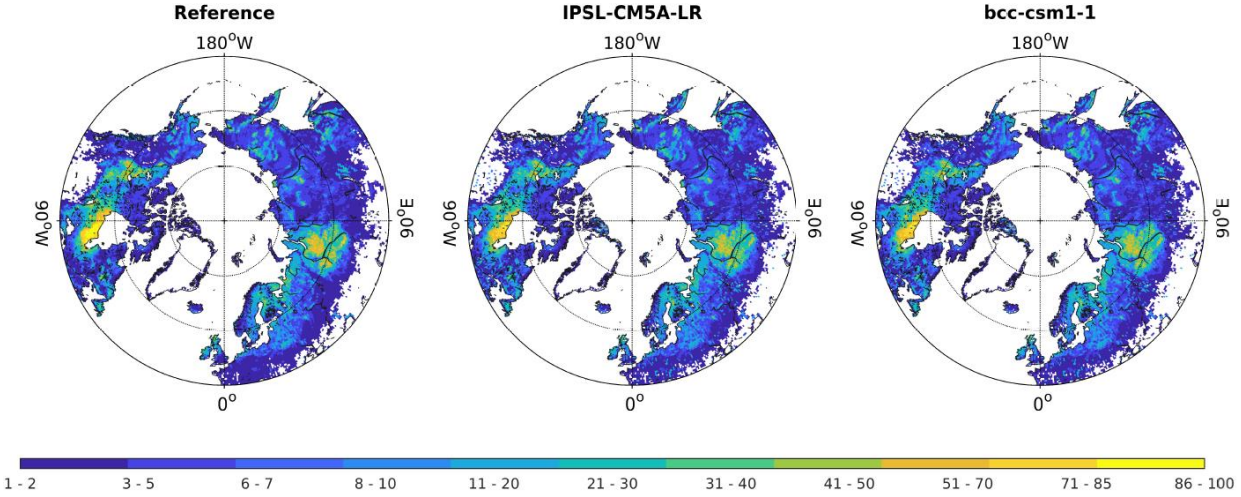
249 **Figure 2.** Comparison between the reference and calibrated wetland abundance (%) during 1940-1990 interpolated with

250 TOPMODEL approach. The reference dataset is the average peatland abundance of three peatland maps (Xu et al., 2018;

251 Hugelius et al., 2020; Melton et al., 2022), and calibration is conducted for IPSL-CM5A-LR and bcc-csm1-1 climate inputs,

252 respectively. The grid cells with less than 1% wetlands are left blank. This is the initial wetland extent for future peatland

253 simulation.

254 **2.3 Peatland simulation**

255 **2.3.1 PTEM revision**

256   The TOPMODEL-interpolated bin WTD is used as an input in peatland simulation. In contrast to the WTD

257 simulation where the grid cell run-on is assumed to be zero (Eq. (11)), the run-on in peatland simulation is calculated with a

258 water balance equation:

259 $\Delta SM = P + R_{on} - R_{off} - B - EET$ (12)

260   Where ΔSM is the difference between soil moisture at two adjacent time steps (i.e., months), and the soil moisture

261 in each month is estimated form the input WTD and the WTD-soil moisture relationship given by Eq. (5-7). The run-off

262 (R_{off}), base flow (B) and evapotranspiration (EET) are calculated in the same way as in WTD simulation. pH values are

263 influential to CH_4 production process and is simulated in both Holocene and future simulations. In the Holocene simulation,

264 soil pH value is calculated as a function of run-on which is solely controlled by peat thickness. In the revision, soil pH is

265 calculated as:

266 $pH = -log_{10}(n^{H^+}/SM)$ (13)

267   Where pH is the soil pH value, n^{H^+} is the number of H^+ particles, and SM is the soil moisture (mm). Notably, on

268 unit area (i.e., $1m^2$), 1mm soil moisture is equal to 1L soil water. Therefore, n^{H^+}/SM calculates the concentration of H^+

269 particles per litter. And the number of H^+ particles is calculated as:

270 $$\Delta H^+ = 10^{-pH_p} \times P + 10^{-pH_{ron}} \times R_{on} - 10^{-pH_w} \times EET - 10^{-pH_0} \times (R_{off} + B) \quad\quad (14)$$

271 Where pH_p is the pH value of precipitation (assumed 5.0), pH_{ron} is the pH value of run-on water (assumed 7.0),
272 pH_w is the pH value of EET water (assumed 7.0), and pH_0 is the pH value of soil water at previous month. The spatially
273 explicit initial pH values are from (Carter and Scholes, 2000).

274 In Holocene simulations, CH4 production is simulated, but since oxidation process is not considered, CH4 emission
275 is not calculated. In this revision, CH4 oxidation is enabled and thereby it is possible to estimate net CH4 emission. The
276 algorithms are documented in Zhuang et al. (2004).

277 **2.3.2 PTEM simulation**

278 In each grid cell, among the 100 bins classified by TWI, the bins that the long-term WTD has ever been shallower
279 than 25cm are classified as 'potential peatlands', which are used for peatland simulation. To be consistent with the WTD
280 simulation, long-term WTD refers to the 50-year moving average of annual WTD. In this study, we assume within each grid
281 cell, the climate conditions are similar and the key control of whether peat exists at sub-grid cell scale is the local WTD
282 influenced by sub-grid topography. Therefore, for all the bins in the same 0.5°×0.5° grid cell, the forcing data, soil texture,
283 elevation and parameters are the same except for the input WTD.

284 In Holocene simulations, the maximum C assimilated by ecosystem parameter (c_{max}) is calibrated for over 2000
285 peat cores and interpolated into the pan-Arctic region (Zhao et al., 2022a). The calibration process reduces the uncertainty
286 from forcing data, other parameters and model structure, and the simulated spatial and temporal pattern of pan-Arctic
287 peatland C stock is consistent with multiple datasets (Zhao et al., 2022a). However, since the hydrology module of PTEM
288 2.2 is revised and peat accumulation and decomposition is sensitive to hydrological processes, using the original parameters
289 could result in considerable bias. In order to make sure the revised PTEM 2.2 simulates consistent C accumulation rate
290 (CAR) with the previous study, a spatially explicit calibration on maximum C assimilated by ecosystem (c_{max}) parameter is
291 conducted.

292 Before calibrating CAR, it is necessary to initialize PTEM 2.2 with reasonable peat conditions. To initialize the
293 simulation, the peat profile in 1940 derived from the Holocene simulation (Zhao et al., 2022a) is used (Figure 3). In
294 particular, the peat profile records the physical property of vertical peat layers including bulk density, organic C density,
295 layer thickness (1cm except for the top layer), fraction of remaining undecomposed organic matter and decomposition rate of
296 undecomposed organic matter at 0°C. This information can be used to estimate the decomposition rate of existing peat given
297 WTD, soil pH and soil temperature (Zhao et al., 2022b).

298 With initial peat profile as an input, c_{max} values are calibrated with PEST (v17.2 for Linux). In particular, within
299 each grid cell, the 50-year average CAR of historical wetland bins (i.e., the bins that are classified as wetlands during 1940-
300 1990) are simulated and averaged to get the grid cell average 50-year peatland CAR. This grid cell average peatland CAR is
301 calibrated against the CAR derived from the Holocene simulation during the same period (SI Figure 5).

302   After calibration, the peat simulation is conducted for all pan-Arctic potential peatland bins during 1940-2300
303   (Figure 2). For the Greenland grid cells not included in the Holocene simulation and thereby have no calibrated c_{max} values,
304   the c_{max} values are interpolated from adjacent grid cells. For the bins not included in the Holocene simulation or not being
305   peatlands before 1990, the peat profile is initialized as 3cm fully decomposed peat. Notably, under different forcing data and
306   warming scenarios, the number and distribution of potential peatland bins are slightly different, which makes the initial pan-
307   Arctic peatland C storage in 1940 slightly different (SI Table 2). When running peat simulation, the forcing input
308   (temperature, precipitation, cloudiness and vapor pressure), soil texture, elevation and parameters are the same as the ones
309   used in the WTD simulation, except for the spatial-explicit c_{max} values.
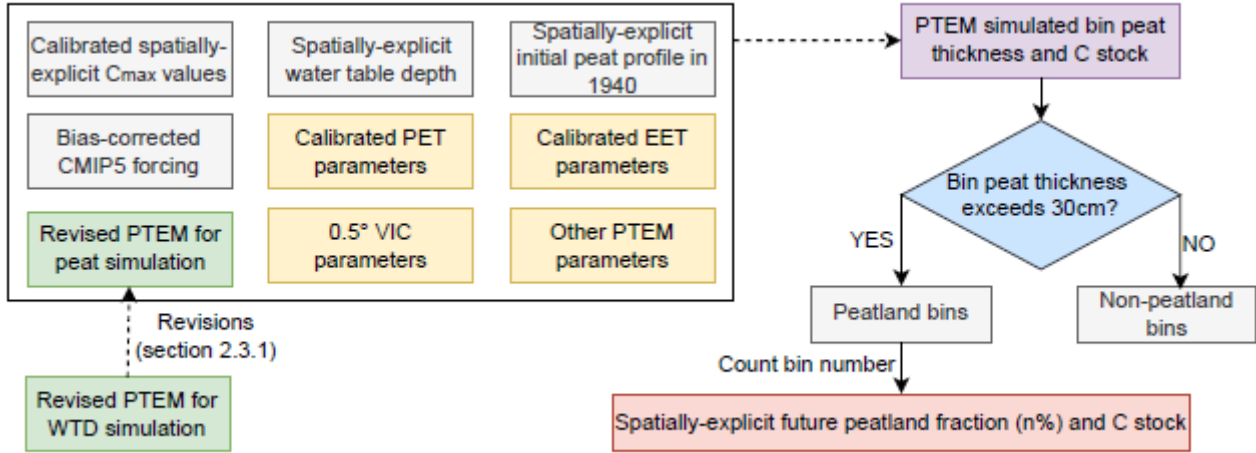
310
311   **Figure 3. Flow chart of Method Section 2.3.2.**
312   **2.3.3. Peat simulation post-processing**
313   After simulation, the simulated results are analyzed in terms of 1) the temporal pattern of pan-Arctic climate
314   dynamics; 2) the temporal pattern of pan-Arctic peatland C stocks and C fluxes; 3) the main drivers of pan-Arctic peatland C
315   dynamics; and 4) the threshold temperature and precipitation needed to transition the peatland from a C sink to a C source.
316   Threshold temperature is calculated with logistic regression:

317    $$f(temp) = \begin{cases} 0 & \text{Net ecosystem productivity} \leq 0 \\ 1 & \text{Net ecosystem productivity} > 0 \end{cases} \quad (15)$$

318   A fitting curve of $f(temp)$ is derived for the pan-Arctic region and for each grid cell. Under sink-source shift, the
319   fitting curve rises from 0 to 1, and the threshold temperature of sink-source shift is determined when $f(temp)$ is 0.5. The
320   threshold precipitation and threshold number of annual unfrozen days is calculated in the same way. In particular, to estimate
321   the number of unfrozen days, the daily temperature is reconstructed from monthly temperature by the algorithms used in
322   Zhao et al. (2022a).
323   **3. Results**
324   **3.1 Warmer and drier pan-Arctic peatlands during 1990-2300**
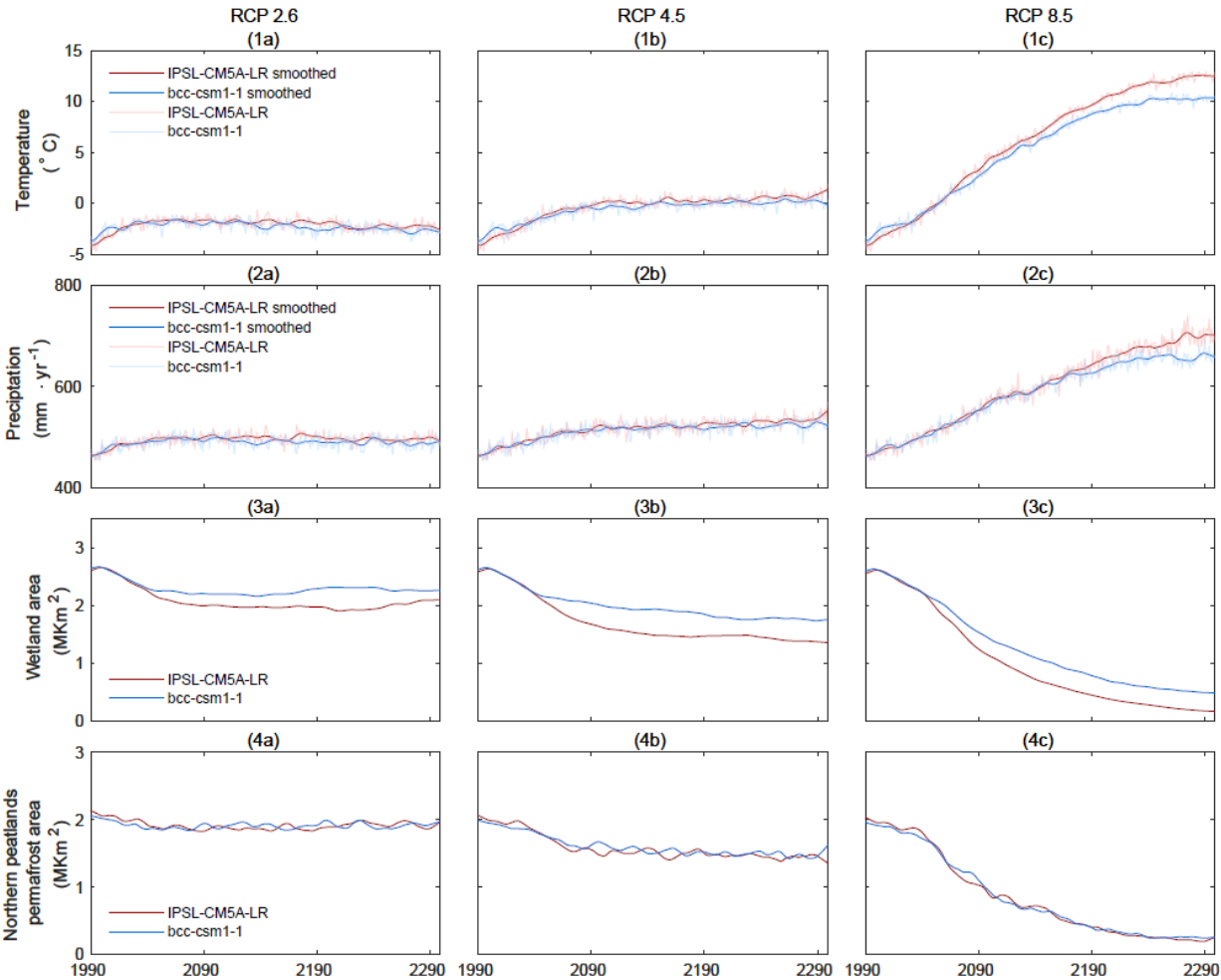
Figure 4. Time series of pan-Arctic annual air temperature (°C), annual precipitation (mm·yr^{-1}), wetland area (Mkm^2) and permafrost area in peatland regions (Mkm^2) during 1990-2300.

Both IPSL-CM5A-LR and bcc-csm1-1 climates show increasing temperature and precipitation during 1990-2300. In particular, under RCP 2.6 and RCP 4.5, temperature increases mostly before 2100 by 2.3-4.1°C and 2.0-3.2°C under IPSL-CM5A-LR and bcc-csm1-1, respectively (Figure 4 1(a-b), SI Table 3). Meanwhile, precipitation increases by 40.7-59.7 mm·yr^{-1} and 38.1-53.9 mm·yr^{-1} for under IPSL-CM5A-LR and bcc-csm1-1 (Figure 4 2(a-b), SI Table 3). During 2100-2300, under RCP 2.6, the temperature decreases by 0.8°C in IPSL-CM5A-LR and by 1.1°C in bcc-csm1-1. Under RCP 4.5, temperature keeps increasing but in a slower rate than before 2100 (IPSL-CM5A-LR: 1.3°C vs. bcc-csm1-1: 0.4°C). Meanwhile, precipitation slightly decreases under RCP 2.6 (IPSL-CM5A-LR: -12.0 mm·yr^{-1} vs. bcc-csm1-1: -5.8 mm·yr^{-1}) while increases under RCP 4.5 (IPSL-CM5A-LR: 29.1 mm·yr^{-1} vs. bcc-csm1-1: 8.5 mm·yr^{-1}) (Figure 4 1(a-b) &2(a-b), SI Table 3). Different from RCP 2.6 and RCP 4.5, the increase in temperature and precipitation under RCP 8.5 is stable during

1990-2200, and slows down after 2200. In particular, under IPSL-CM5A-LR, during 1990-2100 and 2100-2300, temperature increases by 8.4 and 8.1 °C while precipitation increases by 106.1 and 131.7 mm·yr^{-1}. Under bcc-csm1-1, during 1990-2100 and 2100-2300, temperature increases by 7.2 and 6.9 °C while precipitation increases by 100.9 and 198 mm·yr^{-1}, respectively (Figure 4 (1-2)c, SI Table 3).

The result of pan-Arctic wetland shrinking under all scenarios indicates that the increase of precipitation does not compensate the increase of evapotranspiration under warmer climate. Therefore, the pan-Arctic generally becomes drier and WTD becomes deeper (Figure 4 3(a-c), SI Figure 6&7). In particular, during 1990-2100, under IPSL-CM5A-LR, wetland shrinks by 0.6, 0.9 and 1.4 million km^2 under three RCP scenarios. Meanwhile, under bcc-csm1-1, wetland shrinks slightly less by 0.4, 0.6 and 1.2 million km^2 under three RCP scenarios, respectively. During 2100-2300, under both IPSL-CM5A-LR and bcc-csm1-1, wetlands slightly expand by 0.1 million km^2 under RCP 2.6, while under the warmer scenarios, wetland further shrinks by 0.2 and 0.9 million km^2, respectively (Figure 4 3(a-c), SI Table 3).

Following climate warming, permafrost shrink is simulated across the current pan-Arctic peatland region under all scenarios (Figure 4 4(a-c)). In particular, with IPSL-CM5A-LR forcing, under RCP 2.6, 4.5 and 8.5, permafrost shrinks by 0.2, 0.7 and 1.2 million km^2 during 1990-2100 and expands by 0.1, shrinks by 0.1 and 0.5 million km^2, respectively, during 2100-2300. Meanwhile, active layer deepening is simulated in the remaining permafrost region (SI Figure 8). Similarly, with bcc-csm1-1 forcing, under RCP 2.6, 4.5 and 8.5, permafrost shrinks by 0.2, 0.2 and 1.0 million km^2 during 1990-2100 and expands by 0.1, shrinks by 0.1 and 0.6 million km^2, respectively, during 2100-2300 (Figure 4 4(a-c), SI Table 3). Meanwhile, active layer deepening is simulated in the remaining permafrost region under RCP 4.5 and 8.5 (SI Figure 9).

Under RCP 2.6 and 4.5, with both IPSL-CM5A-LR and bcc-csm1-1 forcing, peatlands (i.e., the region with peat thickness >= 30cm) area expands during 1990-2300 (Figure 5). In particular, the new peat area expands by 0.1 to 0.2 million km^2, while the old peat area is stable (SI Table 3). Under RCP 8.5, however, peatland area shrinks. In particular, although new peat land area expands by 0.1 million km^2, the old peatland area shrinks by 0.1 to 0.4 million km^2, causing total peatland area decrease (Figure 5, SI Table 3).
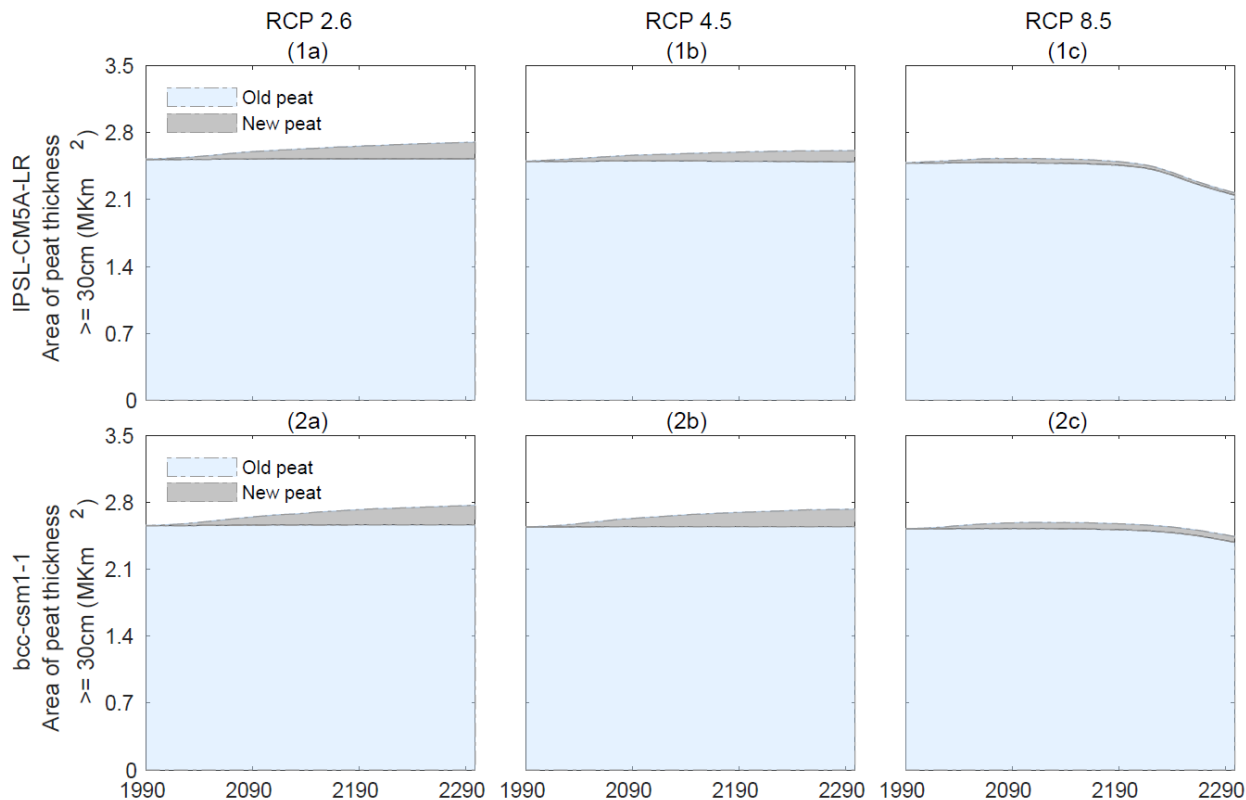
Figure 5. Time series of pan-Arctic old and new peatland area (million km^2) during 1990-2300.

3.2 Pan-Arctic C stocks and fluxes under climate change

3.2.1 Before 2100

With WTD becomes deeper, active layer depth becomes deeper and permafrost extent shrink, it is reasonable that decomposition increases during 1990-2100 under all scenarios (Figure 6 3&4 (a-c), Table 2). Meanwhile, NPP slightly decreases with IPSL-CM5A-LR forcing while increases with bcc-csm1-1 forcing (Figure 6 2(a-c), Table 2). In PTEM 2.2, NPP is primarily influenced by temperature and nitrogen availability, and available nitrogen mainly comes from net N mineralization. In all scenarios, net N mineralization rate increases (negative values indicate higher net N mineralization) during 1990-2100 (SI Figure 10), indicating more available N for vegetation. The increase in both N availability and temperature can not explain the reason for NPP decrease. However, NPP decrease can be explained by the shift in PFTs. In particular, during 1990-2100, with water table becomes deeper, the dominance of herbaceous plants is gradually replaced by woody plants (i.e., shrubs and trees) that can thrive under drier conditions (SI Figure 11). In PTEM 2.2, compared with herbaceous plants, woody plants require more nitrogen for production. Therefore, although N availability increases, the increase is not sufficient for woody plants to maintain as high NPP as herbaceous plants and the overall NPP decreases.

377
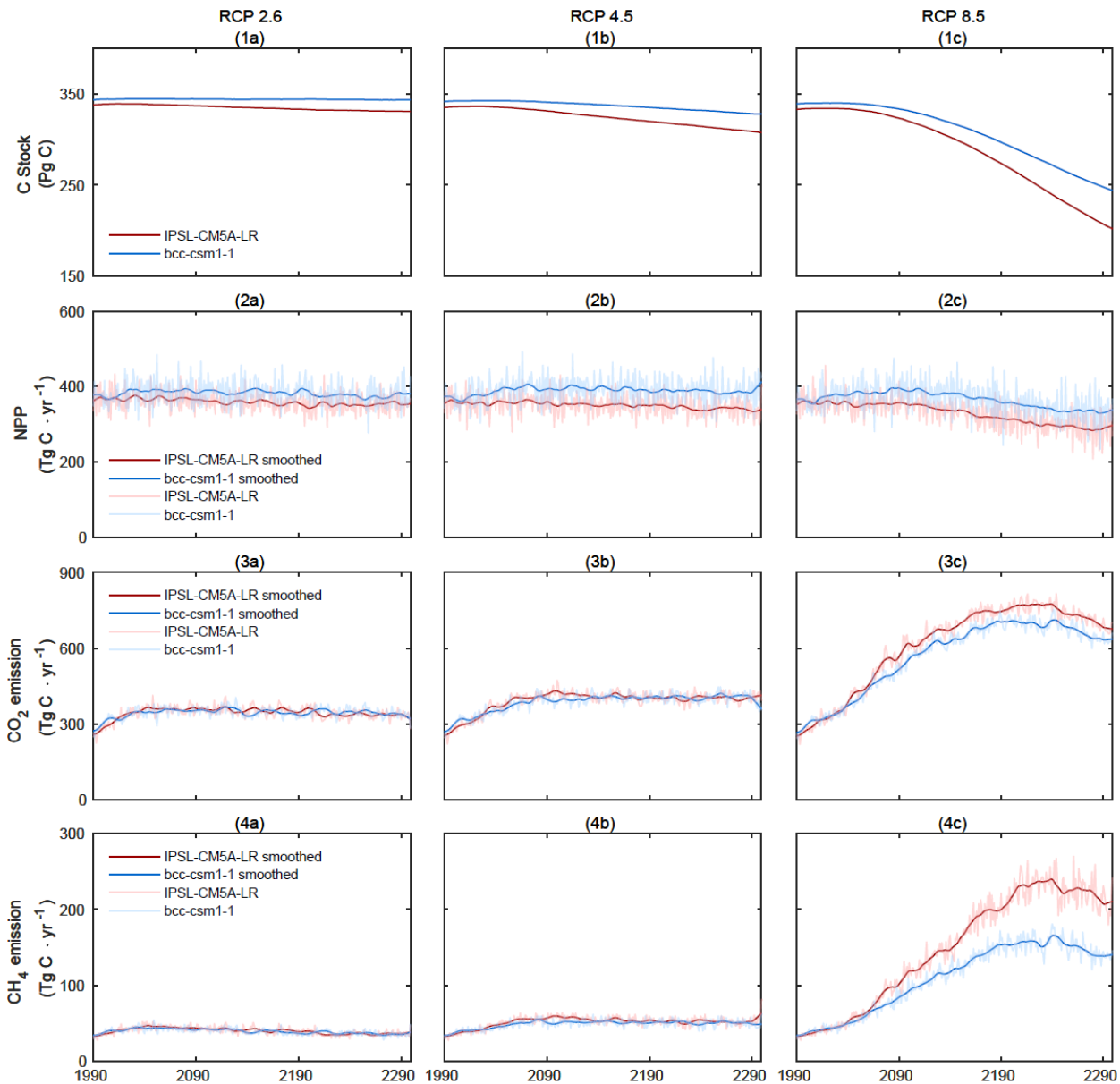
Figure 6. Time series of pan-Arctic peatland C storage (vegetation and soil, Pg C), NPP (TgC·yr⁻¹), CO₂ emissions from soil heterotrophic respiration (TgC·yr⁻¹) and CH₄ emissions (TgC·yr⁻¹) during 1990-2300.

In all scenarios except for bcc-csm1-1 RCP 2.6, the increase in decomposition overrides the increase in NPP and thereby C stock decreases (Figure 6 1(a-c), Table 2). In particular, with ISP-CM5A-LR forcing, by 2100, C stock decreases by 1.3, 5.2 and 13.3 Pg C under RCP 2.6, 4.5 and 8.5, respectively. With bcc-csm1-1 forcing, by 2100, C stock increases by 0.8 Pg C under RCP 2.6, while decreases by 1.2 and 7.8 Pg C under RCP 4.5 and 8.5, respectively (Figure 6 1(a-c), Table 2). Notably, although pan-Arctic peatlands are C sinks during 1990-2100 under bcc-csm1-1 RCP 2.6, the sink is much lower

385 than that during 1940-1990 with CAR decreases by 29.1 gC·m^{-2}·yr^{-1}. Furthermore, this difference is larger in the other

386 scenarios (IPSL-CM5A-LR: 35.5-63.5 gC·m^{-2}·yr^{-1}, bcc-csm1-1: 34.6-50.0 gC·m^{-2}·yr^{-1}) (SI Figure 12&13, Table 3).

387 **Table 2.** Pan-Arctic total C stock and annual C fluxes in 1990, 2100 and 2300

		IPSL-CM5A-LR			bcc-csm1-1		
		RCP 2.6	RCP 4.5	RCP 8.5	RCP 2.6	RCP 4.5	RCP 8.5
C stock (Pg C)	1990	338.1	335.4	333.3	343.7	341.8	339.3
	2100	336.8	330.2	320.0	344.5	340.6	331.5
	2300	330.9	307.7	201.7	343.8	328.0	243.9
NPP (TgC·yr^{-1})	1990	362.2	355.0	352.4	377.6	373.1	366.2
	2100	361.4	348.2	350.9	390.7	391.5	387.7
	2300	354.4	340.0	297.5	381.4	413.2	339.0
CO_2 emission (TgC·yr^{-1})	1990	257.9	254.3	252.5	272.2	269.2	265.8
	2100	357.0	430.1	618.5	352.7	389.9	558.0
	2300	320.0	413.5	676.1	321.1	359.5	636.5
CH_4 emission (TgC·yr^{-1})	1990	31.8	31.7	31.7	33.8	33.7	33.7
	2100	42.4	59.2	118.8	42.3	49.5	92.9
	2300	37.9	62.9	210.7	37.9	48.5	140.5

388 * C stock includes both soil and vegetation C.

389

390 **Table 3.** Pan-Arctic peatlands C accumulation rate during four time periods

		IPSL-CM5A-LR			bcc-csm1-1		
		RCP 2.6	RCP 4.5	RCP 8.5	RCP 2.6	RCP 4.5	RCP 8.5
C accumulation rate (gC·m^{-2}·yr^{-1})	1940-1990	32.5	31.9	31.8	32.1	32.1	31.5
	1990-2090	-3.0	-13.0	-33.5	3.0	-2.5	-18.5
	2090-2190	-12.3	-38.7	-169.0	-1.1	-18.2	-122.2
	2190-2290	-7.6	-36.9	-227.3	-1.9	-23.1	-163.8

391 * C accumulation rate is averaged from all grid cells weighted by the spatially-explicit peatland area.

392

393 **3.2.2 During 2100-2300**

394 During 2100-2300, the decrease in decomposition rate is simulated in RCP 2.6 and 4.5 with both forcing, while

395 decomposition rate becomes higher under RCP 8.5 (Table 2). Under RCP 2.6, the decrease in decomposition is driven by the

396 colder and wetter climate (Figure 4), while with IPSL-CM5A-LR forcing the decrease of C stock also influences

397 decomposition rate negatively. In contrast, under RCP 4.5 where climate becomes warmer and drier, the decrease in

398 decomposition rate is mostly driven by the lower C stock available for decomposition. However, under RCP 8.5 where the

399 climate change is more severe, the positive effect of warming and drying overrides the negative effect of insufficient C stock

400 and thereby decomposition rate keeps increasing (Figure 6 3&4(a-c), Table 2).

401   During 2100-2300, NPP in all scenarios decrease except for bcc-csm1-1 RCP 4.5 (Figure 6 2(a-b), Table 2). For

402 both forcing, under RCP 2.6 and 4.5, PFT distribution is stable after 2100 (SI Figure 11 1&2(a-b)). Therefore, NPP is driven

403 by the balance of net N mineralization and temperature. For bcc-csm1-1 RCP 4.5, the positive effect of temperature

404 overrides the negative effect of decreasing net N mineralization, while the opposite is found in the other scenarios (SI Figure

405 10). Under RCP 8.5, with further herbaceous-woody switch and decrease in net N mineralization, NPP decreases with both

406 forcing (Figure 6 2(c), Table 2). With NPP decrease and decomposition increase, pan-Arctic peatlands are C sources under

407 all scenarios. In particular, with IPSL-CM5A-LR forcing, under RCP 2.6, 4.5 and 8.5, pan-Arctic peatlands are sources of

408 5.9, 22.5 and 118.3 Pg C, respectively, while these values are 0.7, 12.6 and 87.6 Pg C with bcc-csm1-1 forcing, respectively

409 (Figure 6 1(a-c), Table 2). During 2100-2300, CAR is lower than that during the 21st century. In particular, under RCP 2.6,

410 4.5 and 8.5, CAR further decreases by 4.6-9.3 $gC·m^{-2}·yr^{-1}$, 23.9-25.7 $gC·m^{-2}·yr^{-1}$ and 135.5-193.8 $gC·m^{-2}·yr^{-1}$ with IPSL-

411 CM5A-LR forcing and 4.1-4.9 $gC·m^{-2}·yr^{-1}$, 15.7-20.6 $gC·m^{-2}·yr^{-1}$ and 103.7-145.3 $gC·m^{-2}·yr^{-1}$ with bcc-csm1-1 forcing,

412 respectively (SI Figure 12&13, Table 3).

413 **3.3 Pan-Arctic peatlands C sinks in response to climate change**

414   For both IPSL-CM5A-LR and bcc-csm1-1 forcings, the positive correlation between temperature and precipitation

415 is found at the pan-Arctic scale (Table 4). In particular, with 1°C annual temperature increase, the annual precipitation

416 increases by 13.84-15.33 $mm·yr^{-1}$ in IPSL-CM5A-LR forcing and 13.78-14.59 $mm·yr^{-1}$ in bcc-csm1-1 forcing. The

417 correlation has higher R^2 values in warmer scenarios. The positive correlation between temperature and precipitation is

418 mostly found in Eurasia and northeast America, where the R^2 values are also higher than the other region (SI Figure 14&15).

419   The negative correlation between temperature and pan-Arctic peatland C sink activity is found in both forcing

420 scenarios (Table 4). In particular, with 1°C annual temperature increase, pan-Arctic peatland C sink decreases by 40.46-

421 46.91 $Tg C·yr^{-1}$ in IPSL-CM5A-LR forcing and 33.27-41.1 $Tg C·yr^{-1}$ in bcc-csm1-1 forcing. The negative effect of

422 temperature is weaker in western Eurasia and Alaska regions, while stronger in the other regions where most of the current

423 peatlands exist (SI Figure 16&17). Due to the close positive correlation between temperature and precipitation, the

424 correlation between precipitation and pan-Arctic peatland C sink is also negative. In particular, with 1mm annual

425 precipitation increase, pan-Arctic peatland C sink decreases by 2.32-3.28 $Tg C·yr^{-1}$ in IPSL-CM5A-LR forcing and 1.85-2.92

426 $Tg C·yr^{-1}$ in bcc-csm1-1 forcing (Table 4). The spatial pattern of precipitation-C sink correlation is consistent with the spatial

427 pattern of temperature-C sink correlation (SI Figure 18&19).

428   At the pan-Arctic scale, a threshold annual temperature and precipitation can be found when peatlands switch from

429 a C sink to a source. In particular, with IPSL-CM5A-LR forcing, the threshold annual temperature is -2.89 - -2.6°C, the

430 corresponding annual unfrozen day number is 169-180 days and the threshold precipitation is 479.59 - 482.55 mm (SI Figure

431 24). With bcc-csm1-1 forcing, the threshold annual temperature is -2.35 - -2.09°C, the corresponding annual unfrozen day

432 number is 176-181 days and the threshold precipitation is 484.69 - 489.02 mm (Table 4, SI Figure 24). The threshold

433 temperature varies spatially with mostly below -3°C in the northern North American and western Eurasia regions and mostly

434 above 1°C in the lower latitude regions (SI Figure 20). Notably, the regions with below -3°C threshold temperature tend to

435 have higher R^2 values (SI Figure 21). The spatial pattern of precipitation threshold is consistent with temperature threshold

436 and the region with 300-500mm annual precipitation threshold has higher R^2 values, mostly seen in northern North

437 American and western Eurasia (SI Figure 22&23).

438 **Table 4.** Relationship between pan-Arctic temperature, precipitation and C sink

Model	RCP 2.6	R^2	RCP 4.5	R^2	RCP 8.5	R^2
Pan-Arctic peatlands C sink capability increases (TgC·yr^{-1}) in response to 1°C annual temperature increase						
IPSL-CM5A-LR	-43.92	0.72	-40.46	0.86	-46.91	0.96
bcc-csm1-1	-34.59	0.51	-33.27	0.76	-41.1	0.96
Pan-Arctic peatlands C sink capability increases (TgC·yr^{-1}) in response to 1mm annual precipitation increase						
IPSL-CM5A-LR	-2.32	0.64	-2.47	0.78	-3.28	0.92
bcc-csm1-1	-1.85	0.46	-2.06	0.73	-2.92	0.94
Annual temperature threshold of C sink-source conversion						
IPSL-CM5A-LR	-2.89 (180*)	0.57	-2.72 (179*)	0.9	-2.6 (169*)	0.86
bcc-csm1-1	-2.35 (181*)	0.16	-2.12 (184*)	0.64	-2.09 (176*)	0.81
Annual precipitation threshold of C sink-source conversion						
IPSL-CM5A-LR	479.59	0.51	482.42	0.86	482.55	0.84
bcc-csm1-1	489.02	0.16	485.5	0.63	484.69	0.79
Annual precipitation increase (mm) in response to 1°C annual temperature increase						
IPSL-CM5A-LR	15.33	0.74	14.71	0.9	13.84	0.98
bcc-csm1-1	13.78	0.61	14.59	0.85	13.78	0.98

439 * Values are the number of unfrozen days corresponding with the threshold temperature.

440 **4. Discussion**

441 **4.1 Wetlands and permafrost dynamics under climate change**

442 Wetlands loss is closely related to climate change and human activities. In particular, the loss has been found

443 globally since 1700AD, with 64-71% loss since 1900 AD (Davidson, 2014). Similarly, a more recent study has found 33%

444 of the global wetland loss as of 2009, with 45% in Europe and 8% in North America (Hu et al., 2017). In addition, regional

445 studies also report different scales of wetlands loss in China and coastal regions (Li et al., 2018; Niu et al., 2012). To date,

446 not many studies focus on future wetland extent simulations and the inconsistency among current wetland extent datasets

447 exists (Loveland et al., 2000; Friedl et al., 2002; Lehner and Döll, 2004; Bartholomé and Belward, 2005). Similar to this

study, one study highlighted the vulnerability of Arctic wetland extent in the 21st century due to permafrost thaw, although most of the permafrost Arctic wetlands can remain stable under RCP 2.6 until at least 2100 (Kåresdotter et al., 2021).

The active layer depth simulated by PTEM 2.2 is compared with two datasets derived from satellite data and models, covering pan-Arctic region and Alaska, respectively (Obu et al., 2020; Yi and Kimball, 2020). The correlation with pan-Arctic dataset (2001-2018) is higher than the correlation with Alaska dataset, while the overall estimation is consistent between our study and two regional datasets (SI Table 4&5). Consistent with our study, Smith et al. (2022) found deepening active layer depth since the 1990s in the permafrost region, indicating permafrost thaw could continue in warmer future and possibly in a higher rate. The permafrost thaw progress in the 21st century agrees with the dynamics simulated by CCSM4 model, suggesting that the CCSM4 permafrost area shrinks by 64% by 2100 under RCP 8.5 compared to our estimation of 53-60% in this study (Lawrence et al., 2012).

4.2 Future productivity and decomposition in northern peatlands

In this study, NPP does not always increase under warmer climate due to PFT switch and net N mineralization rate limiting. The overall trend of pan-Arctic peatland PFT switch is the expansion of woody plants and shrink of herbaceous plants (SI Figure 11). A previous study found that peatland WTD deepening benefits shrub dominance while suppresses forbs and mosses (Mäkiranta et al., 2018). Meanwhile, shrub expansion is reported in Alaska, Siberian and across the pan-Arctic region under historical climate warming (Tape et al., 2006; Blok et al., 2010). Furthermore, the simulation based on LPJ-GUESS also predicts higher proportion of shrub NPP in lower latitude regions due to high insolation and deep WTD (Chaudhary et al., 2020). These studies support our findings that the future warmer and drier condition is the driver for PFT switch and benefits woody plants. Notably, the fraction of woody plants could be overestimated because the PFTs in the potential peatlands are included, where the WTD is usually lower than the existing peatlands and is more suitable for woody plants (SI Figure 11). In the previous PTEM simulation for 15ka BP-1990, when these potential peatlands are not included and WTD is not derived from TOPMODEL, the fraction of herbaceous plants is generally higher than the fraction in this study (Zhao et al., 2022b).

In PTEM 2.2, the net N mineralization rate is related to soil moisture (Zhao et al., 2022b). Therefore, whether future peatlands become more nutrient rich depends on the balance between the positive effect of higher temperature and the negative effect of lower soil moisture. A site-level study on ombrotrophic bog has found increased plant available ammonium under multi-year warming treatment (Iversen et al., 2022). The negative effect of drier soil overwhelms the influence of temperature and thereby net N mineralization rate decrease under RCP 8.5 after 2100 (SI Figure 10). Under a N limiting condition, the modelling study with LPX-Bern 1.0 found peatlands switch from a C sink to a source under RCP 8.5 with slow NPP increase, which is consistent with our simulation with bcc-csm1-1 forcing (Spahni et al., 2013).

Warming affects decomposition mainly in three ways. First, there is higher decomposition rate due to the lower WTD under warming climate conditions (Huang et al., 2021). Second, higher temperature also enhances decomposition more than productivity (Tang et al., 2022). Third, in high latitude regions, soil C decomposition rate is likely to increase under warmer climate and permafrost thaw conditions (Yokohata et al., 2020; Schneider Von Deimling et al., 2015; Gasser

482 et al., 2018; Macdougall and Knutti, 2016; Schuur et al., 2015). In the warming future, the estimation of CO_2 release under

483 RCP 2.6 tends to be higher than the values estimated from other models (by 2100: 54.7-54.8 Pg C in this study vs. 20-58 Pg

484 C in literature; by 2300: 131.2-131.3 Pg C in this study vs. 40-98 Pg C in literature, Table 5). However, the estimation under

485 RCP 8.5 is closer (by 2100: 55.2-57.2 Pg C in this study vs. 42-141 Pg C in literature; by 2300: 222.2-247.6 Pg C in this

486 study vs. 157-313 Pg C in literature) (Yokohata et al., 2020; Schneider Von Deimling et al., 2015; Gasser et al., 2018) (Table

487 5). The CH_4 emission estimation is also higher than that in Yokohata (2020) by 5-6 Pg C by 2100, while the total C emission

488 is close to the estimation of MacDougall (2016) (55 Pg C vs. 56 Pg C).

489 **Table 5.** Comparison of cumulative C emissions between this study and literature

Emission source	Period	RCP scenario	C release	Region	Source
CO_2 (Pg C)	2100	RCP 2.6	54.7-54.8	pan-Arctic peatlands	This study
			21	permafrost region	Yokohata et al. (2020)
			20-58	permafrost region	Schneider Von Deimling et al. (2015)
			27	permafrost region	Gasser et al. (2018)
		RCP 8.5	55.2-57.2	pan-Arctic peatlands	This study
			47	permafrost region	Yokohata et al. (2020)
			42-141	permafrost region	Schneider Von Deimling et al. (2015)
			59	permafrost region	Gasser et al. (2018)
	2300	RCP 2.6	131.2-131.3	pan-Arctic peatlands	This study
			40-98	permafrost region	Schneider Von Deimling et al. (2015)
			47	permafrost region	Gasser et al. (2018)
		RCP 8.5	222.2-247.6	pan-Arctic peatlands	This study
			157-313	permafrost region	Schneider Von Deimling et al. (2015)
			212	permafrost region	Gasser et al. (2018)
CH_4 (Pg C)	2100	RCP 2.6	6	pan-Arctic peatlands	This study
			1	permafrost region	Yokohata et al. (2020)
		RCP 8.5	7.7-8.4	pan-Arctic peatlands	This study
			1.5	permafrost region	Yokohata et al. (2020)
Total (Pg C)	2100	RCP 2.6	55	pan-Arctic peatlands	This study
			56	permafrost region	Macdougall and Knutti (2016)
		RCP 8.5	62.9-65.6	pan-Arctic peatlands	This study
			48	permafrost region	Yokohata et al. (2020)
			92 ± 17	permafrost region	Schneider Von Deimling et al. (2015)
			102	permafrost region	Macdougall and Knutti (2016)

490

4.3 Northern peatland C sink and source shift

492   Our estimated CAR during 1990-2000 is 19.17-22.73 gC·m^{-2}·yr^{-1}, which is lower than that by Chaudhary et al.

493 (2020) during the same period (33.9 gC·m^{-2}·yr^{-1}). However, our estimated CAR is closer to the core-based Holocene CAR

494 (18.6-22.9 gC·m^{-2}·yr^{-1}) (Yu et al., 2009; Loisel et al., 2014). In this study, the estimated pan-Arctic peatlands annual CH$_4$

495 emissions are 28.7 Tg C·yr^{-1} during 1990-2000, 33.0 Tg C·yr^{-1} during 1990-2000 and 38.5 Tg C·yr^{-1} during 2000-2020. The

496 estimation after 1990 is close to the 36.0 Tg C·yr^{-1} in Kleinen et al. (2020) while larger than 25.0 Tg C·yr^{-1} reconstructed

497 from historical data (Treat et al., 2021). However, the difference between our study and Treat et al. (2021) might result from

498 different peatland coverages used in two studies. Under the peatland coverage of Nichols and Peteet (2019), the CH$_4$

499 emissions in Treat et al. (2021) were 32.3-43.5 Tg C·yr^{-1}, which agrees better with our estimates.

500   Multiple studies have indicated there is a C loss trend of northern ecosystems under warming climate (Hanson et al.,

501 2020; Piao et al., 2008; Helbig et al., 2017). In particular, the peatland experiment in Minnesota, USA suggests that each 1°C

502 of warming increases C loss rate by 31.3 gC·m^{-2}·yr^{-1} (Hanson et al., 2020). Similarly, another site-level study on Canadian

503 boreal-wetland biome shows a decline of CO$_2$ uptake from 25±14 gC·m^{-2}·yr^{-1} to 103±38 gC·m^{-2}·yr^{-1} by 2100 depending on

504 the warming scenarios (Helbig et al., 2017). These studies are consistent with our estimates, suggesting that northern

505 peatlands CAR during 1990-2100 is lower than that during 1940-1990 by 29.1-63.5 gC·m^{-2}·yr^{-1}.

506   At the regional scale, whether northern peatlands will switch from a C sink to C source is still uncertain. For

507 example, Gallego-Sala et al. (2018) indicates northern peatlands are likely to sequester more C under RCP 2.6 and RCP 8.5

508 until 2100. Chaudhary et al. (2020), however, indicates the C sink capacity of northern peatlands will decreases under RCP

509 8.5 after 2050. Similarly, McGuire et al. (2018) suggests northern permafrost region could be C sources after 2100 unless

510 under aggressive climate change mitigation pathways. Furthermore, Qiu et al. (2022) simulates northern peatlands dynamics

511 until 2300, suggesting a sink-source shift under RCP 8.5 while no such shift under RCP 2.6. Although conclusions vary

512 among studies, they generally suggest a higher C source possibility under warmer scenarios, which agrees with the negative

513 correlation between temperature and C sink capacity from this study. Furthermore, the arguments that northern peatlands

514 keep being C sinks under RCP 2.6 (Gallego-Sala et al., 2018; Qiu et al., 2022) is consistent with our study under bcc-csm1-1

515 forcing. However, different from previous works (Gallego-Sala et al., 2018; Qiu et al., 2022; McGuire et al., 2018;

516 Chaudhary et al., 2020), our study predicts northern peatlands to be C sources under RCP 2.6 before 2100 with IPSL-CM5A-

517 LR forcing. In addition, the C sink-source switch will occur before 2100 under RCP 4.5 and RCP 8.5. Except for the future

518 decomposition increase, which is common among model predictions (Yokohata et al., 2020; Schneider Von Deimling et al.,

519 2015; Gasser et al., 2018; Macdougall and Knutti, 2016; Schuur et al., 2015), these differences are mainly due to the

520 suppressed NPP in this study.

521 **5. Conclusions**

522   Northern peatlands responses to future climate change during 1990-2300 are simulated with PTEM. The peatlands

523 shrink or expansion, peat accumulation and decomposition processes are considered. Two sets of CMIP5 forcing data (IPSL-

524 CM5A-LR and bcc-csm1-1) are used to drive the model with three warming scenarios (RCP 2.6, RCP 4.5 and RCP 8.5). We

525 found that wetlands will shrink and permafrost will thaw under all scenarios, indicating pan-Arctic peatlands become

526 warmer and drier. Northern peatland area expands under RCP 2.6 and RCP 4.5 while shrinks under RCP 8.5 due to the

527 shrinkage of the area with over 30cm peat thickness under high decomposition rate. NPP does not always increase with

528 temperature because of PFT switch and N limiting effects. However, both CO_2 and CH_4 emissions increase with temperature

529 due to lower WTD, thawing permafrost and higher temperature. By 2100, northern peatlands will be a minor C sink of 0.8

530 Pg C under RCP 2.6 with bcc-csm1-1 forcing while C sources under other scenarios. During 2100-2300, northern peatlands

531 are C sources under all scenarios, the warmer climate results in the larger C source. There are negative correlations between

532 temperature and northern peatland C sink under all scenarios. The negative correlation between precipitation and northern

533 peatland C sink is also found under all scenarios, while this is likely due to the positive correlation between temperature and

534 precipitation. When pan-Arctic annual temperature is -2.89 - -2.6°C with IPSL-CM5A-LR forcing or -2.35 - -2.09°C with

535 bcc-csm1-1 forcing, the northern peatlands switch from a C sink to a source. Similarly, this threshold for annual precipitation

536 is 479.59 - 482.55 mm with IPSL-CM5A-LR forcing and 484.69 - 489.02 mm with bcc-csm1-1 forcing. Our study highlights

537 the current northern peatlands C sink might shift to a source under future warming and drying climate conditions.

538 **Acknowledgments:**

539 This study is financially supported by an NSF project (1802832).

540 **Coda and data availability:**

541 The data used to reproduce figures in both text and supplementary material, PTEM 2.2 codes, model and samples of running

542 directory can be accessed via Purdue University Research Repository: https://purr.purdue.edu/publications/4139/1.

543 **Author contribution:**

544 Bailu Zhao: model revision, model simulation and manuscript writing.

545 Qianlai Zhuang: project design and manuscript revision.

546 There is no competing interests between the authors.

547

548 **References**

549

550 Allen, R. G., Pereira, L. S., Raes, D., and Smith, M.: Crop evapotranspiration - Guidelines for computing crop water
551   requirements - FAO Irrigation and drainage paper 56, 1998.
552 Bartholomé, E. and Belward, A. S.: GLC2000: a new approach to global land cover mapping from Earth observation data,
553   International Journal of Remote Sensing, 26, 1959-1977, 10.1080/01431160412331291297, 2005.
554 Beven, K. J. and Kirkby, M. J.: A physically based, variable contributing area model of basin hydrology / Un modèle à base
555   physique de zone d'appel variable de l'hydrologie du bassin versant, Hydrological Sciences Bulletin, 24, 43-69,
556   10.1080/02626667909491834, 1979.
557 Blok, D., Heijmans, M. M. P. D., Schaepman-Strub, G., Kononov, A. V., Maximov, T. C., and Berendse, F.: Shrub
558   expansion may reduce summer permafrost thaw in Siberian tundra, Global Change Biology, 16, 1296-1305,
559   https://doi.org/10.1111/j.1365-2486.2009.02110.x, 2010.
560 Bohn, T. J., Podest, E., Schroeder, R., Pinto, N., McDonald, K. C., Glagolev, M., Filippov, I., Maksyutov, S., Heimann, M.,
561   Chen, X., and Lettenmaier, D. P.: Modeling the large-scale effects of surface moisture heterogeneity on wetland carbon
562   fluxes in the West Siberian Lowland, Biogeosciences, 10, 6559-6576, 10.5194/bg-10-6559-2013, 2013.
563 Brooks, R. H.: HYDRAULIC PROPERTIES OF POROUS MEDIA, Ph.D., Colorado State University, Ann Arbor, 101 pp.,
564   1965.

565 Carter, A. J. and Scholes, R. J.: SoilData v2.0: Generating a Global Database of Soil Properties CSIR Environmentek,
566   Pretoria, South Africa, 2000.
567 Chaudhary, N., Miller, P. A., and Smith, B.: Modelling past, present and future peatland carbon accumulation across the pan-
568   Arctic region, Biogeosciences, 14, 4023-4044, 10.5194/bg-14-4023-2017, 2017.
569 Chaudhary, N., Westermann, S., Lamba, S., Shurpali, N., Sannel, A. B. K., Schurgers, G., Miller, P. A., and Smith, B.:
570   Modelling past and future peatland carbon dynamics across the pan-Arctic, Global Change Biology, n/a,
571   10.1111/gcb.15099, 2020.
572 Davidson, N. C.: How much wetland has the world lost? Long-term and recent trends in global wetland area, Marine and
573   Freshwater Research, 65, 934-941, https://doi.org/10.1071/MF14173, 2014.
574 Fan, Y., Li, H., and Miguez-Macho, G.: Global Patterns of Groundwater Table Depth, Science, 339, 940,
575   10.1126/science.1229881, 2013.
576 FAO/UNESCO: Soil Map of the World, Food and Agriculture Organization of the United Nations, Paris, 1974.
577 Finger Higgens, R. A., Chipman, J. W., Lutz, D. A., Culler, L. E., Virginia, R. A., and Ogden, L. A.: Changing Lake
578   Dynamics Indicate a Drier Arctic in Western Greenland, Journal of Geophysical Research: Biogeosciences, 124, 870-
579   883, https://doi.org/10.1029/2018JG004879, 2019.
580 Finlayson, C. M. and Milton, G. R.: Peatlands, in: The Wetland Book: II: Distribution, Description, and Conservation, edited
581   by: Finlayson, C. M., Milton, G. R., Prentice, R. C., and Davidson, N. C., Springer Netherlands, Dordrecht, 227-244,
582   10.1007/978-94-007-4001-3_202, 2018.
583 Franchini, M. and Pacciani, M.: Comparative analysis of several conceptual rainfall-runoff models, Journal of Hydrology,
584   122, 161-219, https://doi.org/10.1016/0022-1694(91)90178-K, 1991.
585 Friedl, M. A., McIver, D. K., Hodges, J. C. F., Zhang, X. Y., Muchoney, D., Strahler, A. H., Woodcock, C. E., Gopal, S.,
586   Schneider, A., Cooper, A., Baccini, A., Gao, F., and Schaaf, C.: Global land cover mapping from MODIS: algorithms
587   and early results, Remote Sensing of Environment, 83, 287-302, https://doi.org/10.1016/S0034-4257(02)00078-0, 2002.
588 Gallego-Sala, A. V., Charman, D. J., Brewer, S., Page, S. E., Prentice, I. C., Friedlingstein, P., Moreton, S., Amesbury, M. J.,
589   Beilman, D. W., Björck, S., Blyakharchuk, T., Bochicchio, C., Booth, R. K., Bunbury, J., Camill, P., Carless, D.,
590   Chimner, R. A., Clifford, M., Cressey, E., Courtney-Mustaphi, C., De Vleeschouwer, F., de Jong, R., Fialkiewicz-
591   Koziel, B., Finkelstein, S. A., Garneau, M., Githumbi, E., Hribjlan, J., Holmquist, J., Hughes, P. D. M., Jones, C., Jones,
592   M. C., Karofeld, E., Klein, E. S., Kokfelt, U., Korhola, A., Lacourse, T., Le Roux, G., Lamentowicz, M., Large, D.,
593   Lavoie, M., Loisel, J., Mackay, H., MacDonald, G. M., Makila, M., Magnan, G., Marchant, R., Marcisz, K., Martínez
594   Cortizas, A., Massa, C., Mathijssen, P., Mauquoy, D., Mighall, T., Mitchell, F. J. G., Moss, P., Nichols, J., Oksanen, P.
595   O., Orme, L., Packalen, M. S., Robinson, S., Roland, T. P., Sanderson, N. K., Sannel, A. B. K., Silva-Sánchez, N.,
596   Steinberg, N., Swindles, G. T., Turner, T. E., Uglow, J., Väliranta, M., van Bellen, S., van der Linden, M., van Geel, B.,
597   Wang, G., Yu, Z., Zaragoza-Castells, J., and Zhao, Y.: Latitudinal limits to the predicted increase of the peatland carbon
598   sink with warming, Nature Climate Change, 8, 907-913, 10.1038/s41558-018-0271-1, 2018.
599 Gandois, L., Hoyt, A. M., Hatté, C., Jeanneau, L., Teisserenc, R., Liotaud, M., and Tananaev, N.: Contribution of Peatland
600   Permafrost to Dissolved Organic Matter along a Thaw Gradient in North Siberia, Environmental Science & Technology,
601   53, 14165-14174, 10.1021/acs.est.9b03735, 2019.
602 Gasser, T., Kechiar, M., Ciais, P., Burke, E. J., Kleinen, T., Zhu, D., Huang, Y., Ekici, A., and OberSteiner, M.: Path-
603   dependent reductions in CO2 emission budgets caused by permafrost carbon release, Nature Geoscience, 11, 830-835,
604   10.1038/s41561-018-0227-0, 2018.
605 GISTEMP-Team: GISS Surface Temperature Analysis (GISTEMP), version 4, NASA Goddard Institute for Space Studies
606   [dataset], 2021.
607 Hamman, J. J., Nijssen, B., Bohn, T. J., Gergel, D. R., and Mao, Y.: The Variable Infiltration Capacity model version 5
608   (VIC-5): infrastructure improvements for new applications and reproducibility, Geosci. Model Dev., 11, 3481-3496,
609   10.5194/gmd-11-3481-2018, 2018.
610 Hanson, P. J., Griffiths, N. A., Iversen, C. M., Norby, R. J., Sebestyen, S. D., Phillips, J. R., Chanton, J. P., Kolka, R. K.,
611   Malhotra, A., Oleheiser, K. C., Warren, J. M., Shi, X., Yang, X., Mao, J., and Ricciuto, D. M.: Rapid Net Carbon Loss
612   From a Whole-Ecosystem Warmed Peatland, AGU Advances, 1, e2020AV000163,
613   https://doi.org/10.1029/2020AV000163, 2020.

Harris, I., Jones, P. D., Osborn, T. J., and Lister, D. H.: Updated high-resolution grids of monthly climatic observations – the CRU TS3.10 Dataset, International Journal of Climatology, 34, 623-642, https://doi.org/10.1002/joc.3711, 2014.

He, F.: SIMULATING TRANSIENT CLIMATE EVOLUTION OF THE LAST DEGLACIATION WITH CCSM3, Atmospheric and Oceanic Sciences, UNIVERSITY OF WISCONSIN-MADISON, Madison, 2011.

Helbig, M., Chasmer, L. E., Desai, A. R., Kljun, N., Quinton, W. L., and Sonnentag, O.: Direct and indirect climate change effects on carbon dioxide fluxes in a thawing boreal forest–wetland landscape, Global Change Biology, 23, 3231-3248, https://doi.org/10.1111/gcb.13638, 2017.

Hu, S., Niu, Z., Chen, Y., Li, L., and Zhang, H.: Global wetlands: Potential distribution, wetland loss, and status, Science of The Total Environment, 586, 319-327, https://doi.org/10.1016/j.scitotenv.2017.02.001, 2017.

Huang, Y., Ciais, P., Luo, Y., Zhu, D., Wang, Y., Qiu, C., Goll, D. S., Guenet, B., Makowski, D., De Graaf, I., Leifeld, J., Kwon, M. J., Hu, J., and Qu, L.: Tradeoff of CO2 and CH4 emissions from global peatlands under water-table drawdown, Nature Climate Change, 11, 618-622, 10.1038/s41558-021-01059-w, 2021.

Hugelius, G., Loisel, J., Chadburn, S., Jackson, R. B., Jones, M., MacDonald, G., Marushchak, M., Olefeldt, D., Packalen, M., Siewert, M. B., Treat, C., Turetsky, M., Voigt, C., and Yu, Z.: Large stocks of peatland carbon and nitrogen are vulnerable to permafrost thaw, Proceedings of the National Academy of Sciences, 117, 20438, 10.1073/pnas.1916387117, 2020.

Hugelius, G., Bockheim, J. G., Camill, P., Elberling, B., Grosse, G., Harden, J. W., Johnson, K., Jorgenson, T., Koven, C. D., Kuhry, P., Michaelson, G., Mishra, U., Palmtag, J., Ping, C. L., O'Donnell, J., Schirrmeister, L., Schuur, E. A. G., Sheng, Y., Smith, L. C., Strauss, J., and Yu, Z.: A new data set for estimating organic carbon storage to 3 m depth in soils of the northern circumpolar permafrost region, Earth Syst. Sci. Data, 5, 393-402, 10.5194/essd-5-393-2013, 2013.

Iversen, C. M., Latimer, J., Brice, D. J., Childs, J., Vander Stel, H. M., Defrenne, C. E., Graham, J., Griffiths, N. A., Malhotra, A., Norby, R. J., Oleheiser, K. C., Phillips, J. R., Salmon, V. G., Sebestyen, S. D., Yang, X., and Hanson, P. J.: Whole-Ecosystem Warming Increases Plant-Available Nitrogen and Phosphorus in an Ombrotrophic Bog, Ecosystems, 10.1007/s10021-022-00744-x, 2022.

Kåresdotter, E., Destouni, G., Ghajarnia, N., Hugelius, G., and Kalantari, Z.: Mapping the Vulnerability of Arctic Wetlands to Global Warming, Earth's Future, 9, e2020EF001858, https://doi.org/10.1029/2020EF001858, 2021.

Kleinen, T., Mikolajewicz, U., and Brovkin, V.: Terrestrial methane emissions from the Last Glacial Maximum to the preindustrial period, Clim. Past, 16, 575-595, 10.5194/cp-16-575-2020, 2020.

Lawrence, D. M., Slater, A. G., and Swenson, S. C.: Simulation of Present-Day and Future Permafrost and Seasonally Frozen Ground Conditions in CCSM4, Journal of Climate, 25, 2207-2225, 10.1175/JCLI-D-11-00334.1, 2012.

Lehner, B. and Döll, P.: Development and validation of a global database of lakes, reservoirs and wetlands, Journal of Hydrology, 296, 1-22, https://doi.org/10.1016/j.jhydrol.2004.03.028, 2004.

Li, X., Bellerby, R., Craft, C., and Widney, S. E.: Coastal wetland loss, consequences, and challenges for restoration, Anthropocene Coasts, 1, 1-15, 10.1139/anc-2017-0001, 2018.

Liang, X., Lettenmaier, D. P., Wood, E. F., and Burges, S. J.: A simple hydrologically based model of land surface water and energy fluxes for general circulation models, Journal of Geophysical Research: Atmospheres, 99, 14415-14428, https://doi.org/10.1029/94JD00483, 1994.

Liu, C., Sun, G., McNulty, S. G., Noormets, A., and Fang, Y.: Environmental controls on seasonal ecosystem evapotranspiration/potential evapotranspiration ratio as determined by the global eddy flux measurements, Hydrol. Earth Syst. Sci., 21, 311-322, 10.5194/hess-21-311-2017, 2017.

Loisel, J., Yu, Z., Beilman, D. W., Camill, P., Alm, J., Amesbury, M. J., Anderson, D., Andersson, S., Bochicchio, C., Barber, K., Belyea, L. R., Bunbury, J., Chambers, F. M., Charman, D. J., De Vleeschouwer, F., Fiałkiewicz-Kozieł, B., Finkelstein, S. A., Gałka, M., Garneau, M., Hammarlund, D., Hinchcliffe, W., Holmquist, J., Hughes, P., Jones, M. C., Klein, E. S., Kokfelt, U., Korhola, A., Kuhry, P., Lamarre, A., Lamentowicz, M., Large, D., Lavoie, M., MacDonald, G., Magnan, G., Mäkilä, M., Mallon, G., Mathijssen, P., Mauquoy, D., McCarroll, J., Moore, T. R., Nichols, J., O'Reilly, B., Oksanen, P., Packalen, M., Peteet, D., Richard, P. J. H., Robinson, S., Ronkainen, T., Rundgren, M., Sannel, A. B. K., Tarnocai, C., Thom, T., Tuittila, E.-S., Turetsky, M., Väliranta, M., van der Linden, M., van Geel, B., van Bellen, S., Vitt, D., Zhao, Y., and Zhou, W.: A database and synthesis of northern peatland soil properties and Holocene carbon and nitrogen accumulation, The Holocene, 24, 1028-1042, 10.1177/0959683614538073, 2014.

663 Loisel, J., Gallego-Sala, A. V., Amesbury, M. J., Magnan, G., Anshari, G., Beilman, D. W., Benavides, J. C., Blewett, J.,
664   Camill, P., Charman, D. J., Chawchai, S., Hedgpeth, A., Kleinen, T., Korhola, A., Large, D., Mansilla, C. A., Müller, J.,
665   van Bellen, S., West, J. B., Yu, Z., Bubier, J. L., Garneau, M., Moore, T., Sannel, A. B. K., Page, S., Väliranta, M.,
666   Bechtold, M., Brovkin, V., Cole, L. E. S., Chanton, J. P., Christensen, T. R., Davies, M. A., De Vleeschouwer, F.,
667   Finkelstein, S. A., Frolking, S., Gałka, M., Gandois, L., Girkin, N., Harris, L. I., Heinemeyer, A., Hoyt, A. M., Jones, M.
668   C., Joos, F., Juutinen, S., Kaiser, K., Lacourse, T., Lamentowicz, M., Larmola, T., Leifeld, J., Lohila, A., Milner, A. M.,
669   Minkkinen, K., Moss, P., Naafs, B. D. A., Nichols, J., O'Donnell, J., Payne, R., Philben, M., Piilo, S., Quillet, A.,
670   Ratnayake, A. S., Roland, T. P., Sjögersten, S., Sonnentag, O., Swindles, G. T., Swinnen, W., Talbot, J., Treat, C.,
671   Valach, A. C., and Wu, J.: Expert assessment of future vulnerability of the global peatland carbon sink, Nature Climate
672   Change, 11, 70-77, 10.1038/s41558-020-00944-0, 2021.
673 Loveland, T. R., Reed, B. C., Brown, J. F., Ohlen, D. O., Zhu, Z., Yang, L., and Merchant, J. W.: Development of a global
674   land cover characteristics database and IGBP DISCover from 1 km AVHRR data, International Journal of Remote
675   Sensing, 21, 1303-1330, 10.1080/014311600210191, 2000.
676 Lu, X. and Zhuang, Q.: Modeling methane emissions from the Alaskan Yukon River basin, 1986–2005, by coupling a large-
677   scale hydrological model and a process-based methane model, Journal of Geophysical Research: Biogeosciences, 117,
678   https://doi.org/10.1029/2011JG001843, 2012.
679 MacDougall, A. H. and Knutti, R.: Projecting the release of carbon from permafrost soils using a perturbed parameter
680   ensemble modelling approach, Biogeosciences, 13, 2123-2136, 10.5194/bg-13-2123-2016, 2016.
681 Mäkiranta, P., Laiho, R., Mehtätalo, L., Straková, P., Sormunen, J., Minkkinen, K., Penttilä, T., Fritze, H., and Tuittila, E.:
682   Responses of phenology and biomass production of boreal fens to climate warming under different water-table level
683   regimes, Glob Chang Biol, 24, 944-956, doi: 10.1111/gcb.13934, 2018.
684 Marthews, T. R., Dadson, S. J., Lehner, B., Abele, S., and Gedney, N.: High-resolution global topographic index values for
685   use in large-scale hydrological modelling, Hydrol. Earth Syst. Sci., 19, 91-104, 10.5194/hess-19-91-2015, 2015.
686 McGuire, A. D., Lawrence, D. M., Koven, C., Clein, J. S., Burke, E., Chen, G., Jafarov, E., MacDougall, A. H., Marchenko,
687   S., Nicolsky, D., Peng, S., Rinke, A., Ciais, P., Gouttevin, I., Hayes, D. J., Ji, D., Krinner, G., Moore, J. C.,
688   Romanovsky, V., Schädel, C., Schaefer, K., Schuur, E. A. G., and Zhuang, Q.: Dependence of the evolution of carbon
689   dynamics in the northern permafrost region on the trajectory of climate change, Proceedings of the National Academy
690   of Sciences, 115, 3882, 10.1073/pnas.1719903115, 2018.
691 Meinshausen, M., Smith, S. J., Calvin, K., Daniel, J. S., Kainuma, M. L. T., Lamarque, J. F., Matsumoto, K., Montzka, S. A.,
692   Raper, S. C. B., Riahi, K., Thomson, A., Velders, G. J. M., and van Vuuren, D. P. P.: The RCP greenhouse gas
693   concentrations and their extensions from 1765 to 2300, Climatic Change, 109, 213, 10.1007/s10584-011-0156-z, 2011.
694 Melton, J. R., Chan, E., Millard, K., Fortier, M., Winton, R. S., Martín-López, J. M., Cadillo-Quiroz, H., Kidd, D., and
695   Verchot, L. V.: A map of global peatland extent created using machine learning (Peat-ML), Geosci. Model Dev.
696   Discuss., 2022, 1-44, 10.5194/gmd-2021-426, 2022.
697 Miao, C., Duan, Q., Sun, Q., Huang, Y., Kong, D., Yang, T., Ye, A., Di, Z., and Gong, W.: Assessment of CMIP5 climate
698   models and projected temperature changes over Northern Eurasia, Environmental Research Letters, 9, 055007,
699   10.1088/1748-9326/9/5/055007, 2014.
700 Müller, J. and Joos, F.: Committed and projected future changes in global peatlands – continued transient model simulations
701   since the Last Glacial Maximum, Biogeosciences, 18, 3657-3687, 10.5194/bg-18-3657-2021, 2021.
702 Nichols, J. E. and Peteet, D. M.: Rapid expansion of northern peatlands and doubled estimate of carbon storage, Nature
703   Geoscience, 12, 917-921, 10.1038/s41561-019-0454-z, 2019.
704 Niu, Z., Zhang, H., Wang, X., Yao, W., Zhou, D., Zhao, K., Zhao, H., Li, N., Huang, H., Li, C., Yang, J., Liu, C., Liu, S.,
705   Wang, L., Li, Z., Yang, Z., Qiao, F., Zheng, Y., Chen, Y., Sheng, Y., Gao, X., Zhu, W., Wang, W., Wang, H., Weng, Y.,
706   Zhuang, D., Liu, J., Luo, Z., Cheng, X., Guo, Z., and Gong, P.: Mapping wetland changes in China between 1978 and
707   2008, Chinese Science Bulletin, 57, 2813-2823, 10.1007/s11434-012-5093-3, 2012.
708 Obu, J., Westermann, S., Barboux, C., Bartsch, A., Delaloye, R., Grosse, G., Heim, B., Hugelius, G., Irrgang, A., Kääb, A.
709   M., Kroisleitner, C., Matthes, H., Nitze, I., Pellet, C., Seifert, F. M., Strozzi, T., Wegmüller, U., Wieczorek, M., and
710   Wiesmann, A.: ESA Permafrost Climate Change Initiative (Permafrost_cci): Permafrost Climate Research Data
711   Package v1., Centre for Environmental Data Analysis [dataset],
712   https://catalogue.ceda.ac.uk/uuid/1f88068e86304b0fbd34456115b6606f, 2020.

Olefeldt, D., Hovemyr, M., Kuhn, M. A., Bastviken, D., Bohn, T. J., Connolly, J., Crill, P., Euskirchen, E. S., Finkelstein, S. A., Genet, H., Grosse, G., Harris, L. I., Heffernan, L., Helbig, M., Hugelius, G., Hutchins, R., Juutinen, S., Lara, M. J., Malhotra, A., Manies, K., McGuire, A. D., Natali, S. M., O'Donnell, J. A., Parmentier, F. J. W., Räsänen, A., Schädel, C., Sonnentag, O., Strack, M., Tank, S. E., Treat, C., Varner, R. K., Virtanen, T., Warren, R. K., and Watts, J. D.: The Boreal–Arctic Wetland and Lake Dataset (BAWLD), Earth Syst. Sci. Data, 13, 5127-5149, 10.5194/essd-13-5127-2021, 2021.

Palmer, M. D., Harris, G. R., and Gregory, J. M.: Extending CMIP5 projections of global mean temperature change and sea level rise due to thermal expansion using a physically-based emulator, Environmental Research Letters, 13, 084003, 10.1088/1748-9326/aad2e4, 2018.

Piao, S., Ciais, P., Friedlingstein, P., Peylin, P., Reichstein, M., Luyssaert, S., Margolis, H., Fang, J., Barr, A., Chen, A., Grelle, A., Hollinger, D. Y., Laurila, T., Lindroth, A., Richardson, A. D., and Vesala, T.: Net carbon dioxide losses of northern ecosystems in response to autumn warming, Nature, 451, 49-52, 10.1038/nature06444, 2008.

Qiu, C., Zhu, D., Ciais, P., Guenet, B., and Peng, S.: The role of northern peatlands in the global carbon cycle for the 21st century, Global Ecology and Biogeography, 29, 956-973, https://doi.org/10.1111/geb.13081, 2020.

Qiu, C., Zhu, D., Ciais, P., Guenet, B., Peng, S., Krinner, G., Tootchi, A., Ducharne, A., and Hastie, A.: Modelling northern peatland area and carbon dynamics since the Holocene with the ORCHIDEE-PEAT land surface model (SVN r5488), Geosci. Model Dev., 12, 2961-2982, 10.5194/gmd-12-2961-2019, 2019.

Qiu, C., Ciais, P., Zhu, D., Guenet, B., Chang, J., Chaudhary, N., Kleinen, T., Li, X., Müller, J., Xi, Y., Zhang, W., Ballantyne, A., Brewer, S. C., Brovkin, V., Charman, D. J., Gustafson, A., Gallego-Sala, A. V., Gasser, T., Holden, J., Joos, F., Kwon, M. J., Lauerwald, R., Miller, P. A., Peng, S., Page, S., Smith, B., Stocker, B. D., Sannel, A. B. K., Salmon, E., Schurgers, G., Shurpali, N. J., Wårlind, D., and Westermann, S.: A strong mitigation scenario maintains climate neutrality of northern peatlands, One Earth, https://doi.org/10.1016/j.oneear.2021.12.008, 2022.

Rawls, W. J., Ahuja, L. R., Brakensiek, D. L., and Shirmohammadi, A.: Infiltration and soil water movement, in, McGraw-Hill Inc., New York, 5.1-5.51, 1992.

Richardson, A. D., Hufkens, K., Milliman, T., Aubrecht, D. M., Furze, M. E., Seyednasrollah, B., Krassovski, M. B., Latimer, J. M., Nettles, W. R., Heiderman, R. R., Warren, J. M., and Hanson, P. J.: Ecosystem warming extends vegetation activity but heightens vulnerability to cold temperatures, Nature, 560, 368-371, 10.1038/s41586-018-0399-1, 2018.Schaperow, J. and Li, D.: VICGlobal: soil and vegetation parameters for the Variable Infiltration Capacity hydrological model (1.6d) [dataset], https://doi.org/10.5281/zenodo.5038653, 2021.

Schneider von Deimling, T., Grosse, G., Strauss, J., Schirrmeister, L., Morgenstern, A., Schaphoff, S., Meinshausen, M., and Boike, J.: Observation-based modelling of permafrost carbon fluxes with accounting for deep carbon deposits and thermokarst activity, Biogeosciences, 12, 3469-3488, 10.5194/bg-12-3469-2015, 2015.

Schuur, E. A. G., McGuire, A. D., Schädel, C., Grosse, G., Harden, J. W., Hayes, D. J., Hugelius, G., Koven, C. D., Kuhry, P., Lawrence, D. M., Natali, S. M., Olefeldt, D., Romanovsky, V. E., Schaefer, K., Turetsky, M. R., Treat, C. C., and Vonk, J. E.: Climate change and the permafrost carbon feedback, Nature, 520, 171-179, 10.1038/nature14338, 2015.

Sheffield, J., Barrett, A., Colle, B., Fernando, D., Fu, R., Geil, K., Hu, Q., Kinter, J., Kumar, S., Langenbrunner, B., Lombardo, K., Long, L., Maloney, E., Mariotti, A., Meyerson, J., Mo, K., Neelin, J., Nigam, S., Pan, Z., and Yin, L.: North American Climate in CMIP5 Experiments. Part I: Evaluation of Historical Simulations of Continental and Regional Climatology*, Journal of Climate, 26, 9209-9245, 10.1175/JCLI-D-12-00592.1, 2013.

Smith, S. L., O'Neill, H. B., Isaksen, K., Noetzli, J., and Romanovsky, V. E.: The changing thermal state of permafrost, Nature Reviews Earth & Environment, 3, 10-23, 10.1038/s43017-021-00240-1, 2022.

Spahni, R., Joos, F., Stocker, B. D., Steinacher, M., and Yu, Z. C.: Transient simulations of the carbon and nitrogen dynamics in northern peatlands: from the Last Glacial Maximum to the 21st century, Clim. Past, 9, 1287-1308, 10.5194/cp-9-1287-2013, 2013.

Stocker, B. D., Spahni, R., and Joos, F.: DYPTOP: a cost-efficient TOPMODEL implementation to simulate sub-grid spatio-temporal dynamics of global wetlands and peatlands, Geosci. Model Dev., 7, 3089-3110, 10.5194/gmd-7-3089-2014, 2014.

Tang, R., He, B., Chen, H. W., Chen, D., Chen, Y., Fu, Y. H., Yuan, W., Li, B., Li, Z., Guo, L., Hao, X., Sun, L., Liu, H., Sun, C., and Yang, Y.: Increasing terrestrial ecosystem carbon release in response to autumn cooling and warming, Nature Climate Change, 12, 380-385, 10.1038/s41558-022-01304-w, 2022.

Tape, K. E. N., Sturm, M., and Racine, C.: The evidence for shrub expansion in Northern Alaska and the Pan-Arctic, Global Change Biology, 12, 686-702, https://doi.org/10.1111/j.1365-2486.2006.01128.x, 2006.

Treat, C. C., Jones, M. C., Brosius, L., Grosse, G., Walter Anthony, K., and Frolking, S.: The role of wetland expansion and successional processes in methane emissions from northern wetlands during the Holocene, Quaternary Science Reviews, 257, 106864, https://doi.org/10.1016/j.quascirev.2021.106864, 2021.

Turunen, J., Tomppo, E., Tolonen, K., and Reinikainen, A.: Estimating carbon accumulation rates of undrained mires in Finland–application to boreal and subarctic regions, The Holocene, 12, 69-80, 10.1191/0959683602hl522rp, 2002.

Wood, E. F., Lettenmaier, D. P., and Zartarian, V. G.: A land-surface hydrology parameterization with subgrid variability for general circulation models, Journal of Geophysical Research: Atmospheres, 97, 2717-2728, https://doi.org/10.1029/91JD01786, 1992.

Xu, J., Morris, P. J., Liu, J., and Holden, J.: PEATMAP: Refining estimates of global peatland distribution based on a meta-analysis, CATENA, 160, 134-140, https://doi.org/10.1016/j.catena.2017.09.010, 2018.

Yi, Y. and Kimball, J. S.: ABoVE: Active Layer Thickness from Remote Sensing Permafrost Model, Alaska, 2001-2015, 10.3334/ORNLDAAC/1760, 2020.

Yokohata, T., Saito, K., Ito, A., Ohno, H., Tanaka, K., Hajima, T., and Iwahana, G.: Future projection of greenhouse gas emissions due to permafrost degradation using a simple numerical scheme with a global land surface model, Progress in Earth and Planetary Science, 7, 56, 10.1186/s40645-020-00366-8, 2020.

Yu, Z., Beilman, D., and Jones, M.: Sensitivity of Northern Peatland Carbon Dynamics to Holocene Climate Change, Washington DC American Geophysical Union Geophysical Monograph Series, 184, 55-69, 10.1029/2008GM000822, 2009.

Zhao, B., Zhuang, Q., and Frolking, S.: Modeling Carbon Accumulation and Permafrost Dynamics of Northern Peatlands Since the Holocene, Journal of Geophysical Research: Biogeosciences, 127, e2022JG007009, https://doi.org/10.1029/2022JG007009, 2022b.

Zhao, B., Zhuang, Q., Treat, C., and Frolking, S.: A Model Intercomparison Analysis for Controls on C Accumulation in North American Peatlands, Journal of Geophysical Research: Biogeosciences, 127, e2021JG006762, https://doi.org/10.1029/2021JG006762, 2022a.

Zhao, R. J., Liu, X. R., and Singh, V. P.: The Xinanjiang model,

Zhuang, Q., McGuire, A. D., O'Neill, K. P., Harden, J. W., Romanovsky, V. E., and Yarie, J.: Modeling soil thermal and carbon dynamics of a fire chronosequence in interior Alaska, Journal of Geophysical Research: Atmospheres, 107, FFR 3-1-FFR 3-26, https://doi.org/10.1029/2001JD001244, 2002.

Zhuang, Q., Melillo, J. M., Kicklighter, D. W., Prinn, R. G., McGuire, A. D., Steudler, P. A., Felzer, B. S., and Hu, S.: Methane fluxes between terrestrial ecosystems and the atmosphere at northern high latitudes during the past century: A retrospective analysis with a process-based biogeochemistry model, Global Biogeochemical Cycles, 18, https://doi.org/10.1029/2004GB002239, 2004.

Zomer, R. J. and Trabucco, A.: Version 3 of the "Global Aridity Index and Potential Evapotranspiration (ET0) Database": Estimation of Penman-Monteith Reference Evapotranspiration. (In Press). [dataset], https://cgiarcsi.community/2019/01/24/global-aridity-index-and-potential-evapotranspiration-climate-database-v3/, 2022.

Supplemental References

Obu, J., Westermann, S., Barboux, C., Bartsch, A., Delaloye, R., Grosse, G., Heim, B., Hugelius, G., Irrgang, A., Kääb, A. M., Kroisleitner, C., Matthes, H., Nitze, I., Pellet, C., Seifert, F. M., Strozzi, T., Wegmüller, U., Wieczorek, M., and Wiesmann, A.: ESA Permafrost Climate Change Initiative (Permafrost_cci): Permafrost Climate Research Data Package v1., Centre for Environmental Data Analysis [dataset], https://catalogue.ceda.ac.uk/uuid/1f88068e86304b0fbd34456115b6606f, 2020.

Yi, Y. and Kimball, J. S.: ABoVE: Active Layer Thickness from Remote Sensing Permafrost Model, Alaska, 2001-2015, 10.3334/ORNLDAAC/1760, 2020.

810   Zhao, B., Zhuang, Q., and Frolking, S.: Modeling Carbon Accumulation and Permafrost Dynamics of Northern Peatlands
811   Since the Holocene, Journal of Geophysical Research: Biogeosciences, 127, e2022JG007009,
812   https://doi.org/10.1029/2022JG007009, 2022b. Zomer, R. J. and Trabucco, A.: Version 3 of the "Global Aridity Index
813   and Potential Evapotranspiration (ET0) Database": Estimation of Penman-Monteith Reference Evapotranspiration. (In
814   Press). [dataset], https://cgiarcsi.community/2019/01/24/globalaridity-index-and-potential-evapotranspiration-climate-
815   database-v3/, 2022.

816